

1 **Holocene climates of the Iberian Peninsula: pollen-based reconstructions of changes in**
2 **the west-east gradient of temperature and moisture**

3 Mengmeng Liu^{1,*}, Yicheng Shen², Penelope González-Sampéris³, Graciela Gil-Romera³,
4 Cajo J. F. ter Braak⁴, Iain Colin Prentice¹, Sandy P. Harrison²

5 1: Department of Life Sciences, Imperial College London, Silwood Park Campus, Buckhurst
6 Road, Ascot SL5 7PY, UK

7 2: Geography & Environmental Science, Reading University, Whiteknights, Reading, RG6
8 6AH, UK

9 3: Instituto Pirenaico de Ecología-CSIC, Avda. Montañana 1005, 50059, Zaragoza, Spain

10 4: Biometris (Applied Mathematics and Applied Statistics Centre), Wageningen University &
11 Research, 6708 PB Wageningen, The Netherlands

12 *: Corresponding author: Mengmeng Liu (m.liu18@imperial.ac.uk)

13 Ms for: *Climate of the Past*

14 **Abstract**

15 The Iberian Peninsula is characterised by a steep west-east moisture gradient today, reflecting
16 the dominance of maritime influences along the Atlantic coast and more Mediterranean-type
17 climate further east. Holocene pollen records from the Peninsula suggest that this gradient was
18 less steep during the ~~early to~~ mid-Holocene, possibly reflecting the impact of orbital changes
19 on circulation and thus regional patterns in climate. Here we use ~~7121~~7214 pollen samples
20 from 117 sites covering part or all of the last 12,000 years to reconstruct changes in seasonal
21 temperature and in moisture across the Iberian Peninsula quantitatively. We show that there is
22 an increasing trend in winter temperature at a regional scale, consistent with known changes in
23 winter insolation. However, summer temperatures do not show the decreasing trend through
24 the Holocene that would be expected if they were a direct response to insolation forcing. We
25 show that summer temperature is strongly correlated with plant-available moisture (α), as
26 measured by the ratio of actual evapotranspiration to equilibrium evapotranspiration, which
27 declines through the Holocene. The reconstructions also confirm that the west-east gradient in
28 moisture was considerably less steep than today during the ~~early to~~ mid-Holocene, indicating
29 that atmospheric circulation changes (possibly driven by orbital changes) have been important
30 determinants of the Holocene climate of the region.

31 1. Introduction

32 The Iberian Peninsula is characterised by a steep west-east gradient in temperature and
33 moisture today, reflecting the dominance of maritime influences along the Atlantic coast and
34 more Mediterranean-type climate further east. Projections of future climate change suggest that
35 the region will become both warmer and drier, but nevertheless show that this west-east
36 differentiation is maintained (Andrade et al., 2021a). The changes in temperature are projected
37 to be larger and the occurrence of extreme temperature episodes more frequent in the south-
38 central and eastern parts of Iberia than in Atlantic coastal areas (Carvalho et al., 2021). Similar
39 gradients are seen in future projections of precipitation change, with largest reductions in
40 precipitation in the south-central region (Andrade et al., 2021b). However, the stability of these
41 west-east gradients during the Holocene has been questioned. In particular, the west-east
42 gradient in moisture appears to have been less pronounced during the middle Holocene (8-4
43 ka) when cooler summers and wetter conditions in the Atlantic zone (e.g. Martínez-Cortizas et
44 al., 2009; Mauri et al., 2015) coincided with the maximum development of mesophytic
45 vegetation further east and south (Aranbarri et al., 2014, 2015; Carrión et al., 2010, 2009;
46 González-Sampériz et al., 2017).

47 ~~However, much of the evidence for Holocene climates is based on qualitative interpretations~~
48 ~~of vegetation changes, generally interpreted as reflecting changes in moisture availability~~
49 ~~(Morellón et al., 2018). Although these records are extensive, they seem to indicate fairly~~
50 ~~complex spatial patterns of change. Iberia was included in the quantitative pollen-based~~
51 ~~reconstructions of European climate through the Holocene (Mauri et al., 2015). However, most~~
52 ~~of the ca 50 sites from Iberia were from the Pyrenees and the inferred patterns across the~~
53 ~~Peninsular are therefore largely extrapolated. Furthermore, quantitative reconstructions of~~
54 ~~summer temperature made at individual sites using chironomid data (Muñoz-Sobrino et al.,~~
55 ~~2013; Tarrats et al., 2018) are not consistent with reconstructed changes based on pollen for~~
56 ~~the same sites. However, much of the evidence for Holocene climates of the Iberian Peninsula~~
57 ~~is based on qualitative interpretations of vegetation changes, generally interpreted as reflecting~~
58 ~~changes in moisture availability (Morellón et al., 2018). These records are extensive and they~~
59 ~~seem to indicate fairly complex spatial patterns of change. (Kaufman et al., (2020) provides~~
60 ~~quantitative reconstructions of summer and winter temperature in their compilation of~~
61 ~~Holocene climate information, but there are only 5 terrestrial sites from the Iberian Peninsula.~~
62 ~~Iberia was also included in the quantitative pollen-based reconstructions of European climate~~

63 through the Holocene (Mauri et al., 2015). However, the geographical distribution of sites
64 included is uneven and a large fraction of the records were from the Pyrenees and the
65 Cantabrian mountains, with additional clustering of sites in coastal regions. Thus, the inferred
66 patterns of climate over most of the central part of the Peninsula are therefore largely
67 extrapolated. (Tarroso et al., (2016) has provided reconstructions of summer and winter
68 temperature and mean annual precipitation since the Last Glacial Maximum for the Iberian
69 Peninsula, by using modern species distribution data to develop climate probability distribution
70 functions (PDFs) and applying these to 31 fossil records. However, although they identified
71 trends in precipitation during the Holocene, the temperature reconstructions do not seem to be
72 reliable since they show no changes through time (9 ~ 3 ka), either for the Iberian Peninsula as
73 a whole or for individual sub-regions, in contra-distinction to the other reconstructions. The
74 current state of uncertainty about Holocene climate changes in Iberia is further exacerbated
75 because quantitative reconstructions of summer temperature made at individual sites using
76 chironomid data (Muñoz Sobrino et al., 2013; Tarrats et al., 2018) are not consistent with
77 reconstructed summer temperatures based on pollen for the same sites.

78 Here we re-examine the trends in summer and winter temperature and plant-available moisture
79 through the Holocene across Iberia, using a new and relatively comprehensive compilation of
80 pollen data (Shen et al., 2021) with age models based on the latest radiocarbon calibration
81 curve (IntCal20: Reimer et al., 2020). We explicitly test whether there are significant
82 differences in the west-east gradient of moisture and temperature through time. We then
83 analyse the relationships between the changes in the three climate variables and how trends in
84 these variables are related to external climate forcing. These analyses allow us to confirm that
85 the west-east gradient in moisture was less steep during the mid-Holocene and indicate the
86 importance of changes in atmospheric circulation in explaining observed patterns of climate
87 change across the region.

88 ~~We analyse how these trends are related to external forcing and quantify whether there are~~
89 ~~significant differences in west-east gradients through time.~~

90 **2. Methods**

91 Multiple techniques have been developed to make quantitative climate reconstructions from
92 pollen (see reviews in Bartlein et al., 2011; Chevalier et al., 2020; Salonen et al., 2011). Modern
93 analogue techniques (MAT: Overpeck et al., 1985) tend to produce rapid shifts in reconstructed

94 values corresponding to changes in the selection of the specific analogue samples, although
95 this tendency is less marked in the conceptually analogous response surface technique (Bartlein
96 et al., 1986). Regression-based techniques, including weighted averaging methods such as
97 Weighted Average Partial Least-Squares (WAPLS: ter Braak and Juggins, 1993), do not
98 produce step-changes in the reconstructions but suffer from the tendency to compress the
99 reconstructions towards the central part of the sampled climate range. However, this tendency
100 can be substantially reduced by accounting for the sampling frequency (fx) and the climate
101 tolerance of the pollen taxa present in the training data set (fxTWA-PLS: Liu et al., 2020).
102 Bayesian approaches have also been applied to derive climate reconstructions from pollen
103 assemblages (Peyron et al., 1998). However, comparison of fxTWA-PLS with the Bayesian
104 model BUMPER (Holden et al., 2017), shows that fxTWA-PLS performs better in capturing
105 the climate of the modern training data set from Europe (Liu et al., 2020).

106 Although fxTWA-PLS has clear advantages over other quantitative reconstructions techniques,
107 there is still a slight tendency towards compression. We have therefore made a further
108 modification to the approach as described in Liu et al. (2020). In the original version of
109 fxTWA-PLS, the fx correction is applied as a weight with the form of $1/fx^2$ in the regression
110 (step 7 in Table 1 in Liu et al., 2020). Here (see Appendix A) we make a further modification
111 of fxTWA-PLS by (a) applying the fx correction separately in both the taxon calculation and
112 the regression (step 2 and 7 in Table 1 in Liu et al., 2020) as a weight with the form of $1/fx$ and
113 (b) applying P-splines smoothing (Eilers and Marx, 2021) in order to reduce the dependence
114 of the fx estimation on bin width. The modified version further reduces the biases at the
115 extremes of the sampled climate range. We used this modified version of fxTWA-PLS to
116 reconstruct three climate variables: mean temperature of the coldest month (MTCO), mean
117 temperature of the warmest month (MTWA) and plant-available moisture represented by α , an
118 estimate of the ratio of actual evapotranspiration to equilibrium evapotranspiration. The
119 individual and joint effects of MTCO, MTWA and α were tested explicitly using canonical
120 correspondence analysis (CCA).

121 The modern pollen training dataset was derived from the SPECIAL Modern Pollen Data Set
122 (SMPDS: Harrison, 2019). The SMPDS consists of relative abundance records from 6458
123 terrestrial sites from Europe, northern Africa, the Middle East and northern Eurasia (SI Figure
124 S1) assembled from multiple different published sources. The pollen records were
125 taxonomically standardized, and filtered (as recommended by Chevalier et al., 2020) to remove

126 obligate aquatics, insectivorous species, introduced species, and taxa that only occur in
127 cultivation. Taxa (mainly herbaceous) with only sporadic occurrences were amalgamated to
128 higher taxonomic levels (genus, sub-family or family) after ensuring consistency with their
129 distribution in climate space. As a result of these amalgamations, the SMPDS contains data on
130 247 pollen taxa. For our analysis, we use the 195 taxa that occur at more than 10 sites.

131 Modern climate data at each of the sites in the training data set were obtained from Harrison
132 (2019). This data set contains climate reconstructions of MTCO, growing degree days above a
133 baseline of 0° C (GDD₀) and a moisture index (MI), defined as the ratio of annual precipitation
134 to annual potential evapotranspiration. The climate at each site was obtained using
135 geographically-weighted regression of the CRU CL v2.0 gridded dataset of modern (1961-
136 1990) surface climate at 10 arc minute resolution (New et al., 2002) in order to correct for
137 elevation differences between each pollen site and the corresponding grid cell. The
138 geographically-weighted regression used a fixed bandwidth kernel of 1.06 ° (~140km) to
139 optimize model diagnostics and reduce spatial clustering of residuals relative to other
140 bandwidths. The climate of each pollen site was then estimated based on its longitude, latitude,
141 and elevation. MTCO and GDD₀ was taken directly from the GWR regression and MI was
142 calculated for each pollen site using code modified from SPLASH v1.0 (Davis et al., 2017)
143 based on daily values of precipitation, temperature and sunshine hours again obtained using a
144 mean-conserving interpolation of the monthly values of each. For this application, we used
145 MTCO directly from the data set but calculated MTWA from MTCO and GDD₀, based on the
146 relationship between MTCO, MTWA and GDD₀ given by Appendix 2 of Wei et al. (2021).
147 We derived α from MI following Liu et al. (2020). The modern training data set provides
148 records spanning a range of MTCO from -42.4 °C to 14.8 °C, of MTWA from 4.2 °C to 33.5
149 °C, and of α from 0.04 to 1.25 (Figure 1, SI Fig. S1).

150 The fossil pollen data from the Iberian Peninsula were compiled by Shen et al. (2021) and the
151 data set (Harrison et al., 2022) was obtained from <https://doi.org/10.17864/1947.000369>. We
152 used a modified version of Tolerance-weighted Weighted Averaging Partial Least Square with
153 a sampling frequency correction (fxTWA-PLS; Liu et al., 2020) to reconstruct three climate
154 variables: mean temperature of the coldest month (MTCO), mean temperature of the warmest
155 month (MTWA) and plant available moisture represented by α , an estimate of the ratio of
156 actual evapotranspiration to equilibrium evapotranspiration. The individual and joint effects of
157 MTCO, MTWA and α were tested explicitly using canonical correspondence analysis (CCA).

158 ~~fxTWA-PLS is a modification of the Weighted Average Partial Least Square (WA-PLS)~~
159 ~~approach. The modification produces less compression of reconstructions towards the centre~~
160 ~~of the climatic range sampled by the training dataset, by accounting for the climatic tolerances~~
161 ~~of individual pollen taxa and the frequency of the sampled climate variable (fx) in the training~~
162 ~~dataset (Liu et al., 2020). The fx-correction is applied as a weight with the form of $1/fx^2$ in the~~
163 ~~regression (step 7 in Table 1 in Liu et al., 2020). Here (see Appendix A) we make a further~~
164 ~~modification of fxTWA-PLS by (a) applying the fx-correction separately in both the taxon~~
165 ~~calculation and the regression (step 2 and 7 in Table 1 in Liu et al., 2020) as a weight with the~~
166 ~~form of $1/fx$ and (b) applying P-splines smoothing (Eilers and Marx, 2021) in order to reduce~~
167 ~~the dependence of the fx-estimation on bin-width. The modified version further reduces the~~
168 ~~biases at the extremes of the sampled climate range.~~

169 ~~The modern pollen training dataset was derived from the SPECIAL Modern Pollen Data Set~~
170 ~~(SMPDS; Harrison, 2019). The SMPDS consists of relative abundance records of the 247 most~~
171 ~~important pollen taxa from 6458 terrestrial sites from Europe, the Middle East and northern~~
172 ~~Eurasia (SI Figure S1). For our analysis, we use the 195 taxa that occur at more than 10 sites.~~
173 ~~Modern climate data at each of the sites in the training data set were obtained from Harrison~~
174 ~~(2019). The fossil pollen data from the Iberian Peninsula were compiled by Shen et al. (2021)~~
175 ~~and obtained from <http://dx.doi.org/10.17864/1947.294>. The taxonomy used by Shen et al.~~
176 ~~(2021) is consistent with that employed in the SMPDS. Shen et al. (2021) provides consistent~~
177 ~~age models for all the records based on the IntCal20 calibration curve (Reimer et al., 2020) and~~
178 ~~the BACON Bayesian age-modelling tool (Blaauw et al., 2021; Blaauw and Christeny, 2011)~~
179 ~~using the supervised modelling approach implemented in the ageR package (Villegas-Diaz et~~
180 ~~al, 2021). We excluded individual pollen samples with large uncertainties (standard error larger~~
181 ~~than 100 years) on the attributed in the new age model. As a result, the climate reconstructions~~
182 ~~are based on a fossil data set of 7384 pollen samples from 117 records covering part or all of~~
183 ~~the last 12,000 years (Figure 2), with 42 individual records provided by the original authors,~~
184 ~~73 records obtained from the European Pollen Database (EPD,~~
185 ~~www.europeanpollendatabase.net) and 2 records from PANGAEA (www.pangaea.de/).~~
186 ~~Details of the records are given in SI Table S1. The average temporal resolution of these records~~
187 ~~is 101 years. ~~We excluded individual pollen samples with large age uncertainties (standard~~~~
188 ~~error larger than 100 years).~~ We then also excluded a few samples where the reconstructed
189 values of α exceed the natural limit of 0 and 1.26. Finally, 7214 samples from 117 records are
190 used for the analyses of the climate reconstructions. ~~As a result, the climate analyses are based~~

191 on a fossil data set of 7121 pollen samples from 117 sites covering part or all of the last 12,000
192 years (Figure 1).

193
194 ~~In addition to examining the reconstructions for individual sites, we constructed composite~~
195 ~~curves for the Iberian Peninsula as a whole. These curves were constructed after binning the~~
196 ~~site-based reconstructions using ± 500 -year bins. We did 1000 bootstrap resampling of the~~
197 ~~reconstructed climate values in each ± 500 -year bin to avoid the influence of a single value or~~
198 ~~a single site on the mean climate value in this bin, and use the standard deviation of the 1000~~
199 ~~values to represent the uncertainty of the mean climate value. We constructed linear regression~~
200 ~~plots to examine the longitudinal and elevational patterns in the reconstructed climate~~
201 ~~variables, and assessed the significance of differences in these trends through time compared~~
202 ~~to 0.5 ka based on p values, with the customary threshold of 0.05.~~ In addition to examining the
203 reconstructions for individual sites, we constructed composite curves for the Iberian Peninsula
204 as a whole. The composite curves provide a way of comparing the relationship between trends
205 in the reconstructed climate changes and insolation changes. The curves were constructed after
206 binning the site-based reconstructions using ± 500 -year bins. We did 1000 bootstrap
207 resampling of the reconstructed climate values in each ± 500 -year bin to avoid the influence of
208 a single value or a single site on the mean climate value in this bin, and use the standard
209 deviation of the 1000 values to represent the uncertainty of the mean climate value. We
210 constructed linear regression plots to examine the longitudinal and elevational patterns in the
211 reconstructed climate variables, and assessed the significance of differences in these trends
212 through time compared to the most recent bin (0.5 ka ± 500 years) based on p values, with the
213 customary threshold of 0.05. We then compared the climate trends with changes in summer
214 and winter insolation.

215 ~~The individual and joint effects of MTCO, MTWA and α were tested explicitly using canonical~~
216 ~~correspondence analysis (CCA).~~

217 **3. Results**

218 The modified version of fxTWA-PLS reproduces the modern climate reasonably well (Table
219 1). The performance is best for MTCO (R^2 0.75, RMSEP 4.70, slope 0.91) but is also good for
220 α (R^2 0.68, RMSEP 0.16, slope 0.78) and MTWA (R^2 0.57, RMSEP 3.47, slope 0.71). The
221 correlations between pollen records and each of the three bioclimate variables, as assessed by

222 CCA, were strong for both modern climate data and fossil reconstructions (Table 2). The
223 variance inflation factor scores are all less than 6, so there are no multicollinearity problems
224 (Table 2). Furthermore, the taxa that contribute most strongly to reconstructing colder/warmer
225 or wetter/drier climates show predictable patterns consistent with their known ecological
226 preferences (SI Table S2).

227 Winters were generally colder than present during the early to mid-Holocene, as shown by the
228 coherent patterns of reconstructed anomalies at individual sites (~~Fig. 2~~[Fig. 3a, 3d](#)). Here
229 “present” means the most recent pollen bin (0.5 ka ± 500 years). The composite curve also
230 shows a general increase in winter temperatures through time (~~Fig. 3~~[Fig. 4a](#)), consistent with
231 the trend in winter insolation (~~Fig. 3~~[Fig. 4d](#)). The composite curve shows that it was ca 4°C
232 cooler than today at 11.5 ka and conditions remained cooler than present until ca 2.5 ka. Winter
233 temperature anomalies show no spatial differentiation between western and eastern Iberia
234 (Table 3, SI Fig. S2). The similarity of the changes compared to present geographically is
235 consistent with the idea that the changes in winter temperature are driven by changes in winter
236 insolation.

237 Summers were somewhat hotter than present in the west and cooler than present in the east
238 during the early and middle Holocene, as shown by the reconstructed anomalies at individual
239 sites (~~Fig. 2~~[Fig. 3b, 3e](#)). This west-east difference could not arise if the changes in summer
240 temperatures were a direct reflection of the insolation forcing (~~Fig. 3~~[Fig. 4e](#)). Indeed, the
241 composite curve shows relatively little change in MTWA (~~Fig. 3~~[Fig. 4b](#)), confirming that there
242 is no direct relationship to insolation forcing (~~Fig. 3~~[Fig. 4e](#)).

243 There is a strong west-east gradient in α at the present day (~~Fig. 4~~[Fig. 2](#)), with wetter conditions
244 in the west and drier conditions in the east. However, the reconstructed anomalies at individual
245 sites (~~Fig. 2~~[Fig. 3c, 3f](#)) suggest that west was drier and the east was wetter than present in the
246 mid-Holocene, resulting in a flatter west-east gradient. The west-east gradient is significantly
247 different from present between 9.5 ~ 3.5 ka (~~Fig. 4~~[Fig. 5](#), Table 3), implying stronger moisture
248 advection into the continental interior during the mid-Holocene. The change in gradient is seen
249 in both high and low elevation sites (SI Fig. S3). There is also significant change in α with
250 elevation between 9.5 ~ 4.5 ka (Table 3, SI Fig. S4).

251 Summer temperatures are strongly correlated with changes in α , both in terms of spatial
252 correlations in the modern data set at a European scale and in terms of spatial and temporal

253 ~~correlations the fossil data set from Iberian Peninsula (Fig. 6). Summer temperatures are~~
 254 ~~strongly correlated with changes in α , both in the modern data set at a European scale and in~~
 255 ~~the fossil data set from Iberia (Fig. 5).~~ The patterns of reconstructed anomalies in MTWA and
 256 α at individual sites are also coherent (Fig. 2 Fig. 3b, 3c, 3e, 3f), showing drier conditions
 257 and hotter summers than present in the west and wetter conditions with cooler summers in the
 258 east during the early to mid-Holocene. The west-east gradient in MTWA was significantly
 259 different from present between 9.5 and 3.5 ka except 8.5 ka (Table 3, SI Fig. S5), roughly the
 260 interval when the gradient in α was also significantly different from present. Again, the change
 261 in the east-west gradient is registered at both high and low elevation sites (SI Fig. S6).
 262 However, there is no significant change in MTWA with elevation except 8.5 and 7.5 ka (Table
 263 3, SI Fig. S7).

264 4. Discussion

265 We have shown that there was a gradual increase in MTCO over the Holocene, both for most
 266 of the individual sites represented in the data set and for Iberia as a whole. Colder winters in
 267 southern Europe during the mid-Holocene (6 ka) are a feature of many earlier reconstructions
 268 (e.g. Cheddadi et al., 1997; Wu et al., 2007). A general warming trend over the Holocene is
 269 seen in gridded reconstructions of winter season (December, January, February) temperatures
 270 as reconstructed using the modern analogue approach by Mauri et al. (2015), although there is
 271 somewhat less millennial-scale variability in these reconstructions (SI Fig. S8). Nevertheless,
 272 their reconstructions show a cooling of 3°C in the early Holocene, ~~are~~ comparable in magnitude
 273 to the ca 4°C cooling at 11.5 ka reconstructed here. Although they show conditions slightly
 274 cooler than present persisting up to 1 ka, the differences are very small (ca 0.5°C) after 2 ka,
 275 again consistent with our reconstructions of MTCO similar to present by 2.5 ka. ~~Quantitative~~
 276 ~~reconstructions of winter temperature are available for 5 terrestrial sites from the Iberian~~
 277 ~~Peninsula in the Kaufman et al. (2020) compilation of Holocene climate information. These~~
 278 ~~sites all show a general trend of winter warming over the Holocene, but the magnitude of the~~
 279 ~~change at some of the individual sites is much larger (ca 10°C) and there is no assessment of~~
 280 ~~the uncertainty on these reconstructions. The composite curve of Kaufman et al. (2020) shows~~
 281 ~~an increasing trend in MTCO through the Holocene but with large uncertainties (SI Fig. S8).~~
 282 ~~Our reconstructed trend in winter temperature is consistent with the changes in insolation~~
 283 ~~forcing at this latitude during the Holocene, and is also consistent with transient climate model~~
 284 ~~simulations of the winter temperature response to changing insolation forcing over the late~~

285 ~~Holocene in this region (SI Fig. S9). Thus, we suggest that changes in winter temperatures are~~
286 ~~a direct consequence of insolation forcing.~~ Quantitative reconstructions of winter temperature
287 for the 5 terrestrial sites from the Iberian Peninsula in the Kaufman et al. (2020) compilation
288 all show a general trend of winter warming over the Holocene, but the magnitude of the change
289 at some of the individual sites is much larger (ca 10°C) and there is no assessment of the
290 uncertainty on these reconstructions. The composite curve of Kaufman et al. (2020) shows an
291 increasing trend in MTCO through the Holocene although with large uncertainties (SI Fig. S8).
292 In contrast to the consistency of the increasing trend in MTCO during the Holocene between
293 our reconstructions and those of Mauri et al. (2015) and Kaufman et al. (2020), there is no
294 discernible trend in MTCO during the Holocene reconstruction of (Tarroso et al. (2016).
295 Indeed, there is no significant change in their MTCO values after ca 9 ka, either for the
296 Peninsula as a whole (SI Fig. S8) or for any of the four sub-regions they considered. Our
297 reconstructed trend in winter temperature is consistent with the changes in insolation forcing
298 at this latitude during the Holocene, and is also consistent with transient climate model
299 simulations of the winter temperature response to changing insolation forcing over the late
300 Holocene in this region (SI Fig. S9). Thus, we suggest that changes in winter temperatures are
301 a direct consequence of insolation forcing.

302 We have shown that there is no overall trend in MTWA during the Holocene. According to our
303 reconstructions, summer temperatures fluctuated between ca 0.5°C above or below modern
304 temperature. The lack of coherent trend in MTWA is consistent with the gridded
305 reconstructions of summer (June, July, August) temperature in the Mauri et al. (2015) data set
306 and also with the 5 terrestrial sites from Iberia included in the Kaufman et al. (2020) data set.
307 However, the patterns shown in the three data sets are very different from one another. Mauri
308 et al. (2015) suggest the early Holocene was colder than today, and although temperatures
309 similar to today were reached at 9 ka, most of the Holocene was characterised by cooler
310 summers. Kaufman et al. (2020), however, showed warmer than present conditions during the
311 early Holocene although they also show cooler conditions during the later Holocene. The
312 differences between the three data sets probably reflect differences in the number of records
313 used, but the lack of coherency points to there not being a strong, regionally coherent signal of
314 summer temperature changes during the Holocene. Tarroso et al. (2016) also showed no
315 significant changes in MTWA after ca 9 ka (SI Fig. S8).

316 The chironomid record from Laguna de la Roya covers the late glacial and terminates at 10.5

317 ka (Muñoz Sobrino et al., 2013). The reconstructed July temperature during the early Holocene
318 is ca 12~13 °C, which is considerably cooler than today at this site. However, the authors
319 caution that these samples have poor analogues and the record should be interpreted with
320 caution. Chironomid-based reconstructions of July temperature at Basa de la Mora (Tarrats et
321 al., 2018), a high elevation site in the Pyrenees, indicate temperatures within $\pm 0.5^\circ \text{C}$ of the
322 modern during the early to mid-Holocene (10~6 ka), similar to our regional composite
323 reconstructions. However, they show persistently conditions cooler than present by ca 1.5 °C
324 between 4.5 and 2 ka ~~they show a persistent cooling of 1.5 °C compared to present between 4.5~~
325 ~~and 2 ka~~, not seen in ~~these~~ our reconstructions. Furthermore, direct comparison of our
326 reconstructions of MTWA at Basa de la Mora (SI ~~Fig. S10~~ Fig. S11) to the chironomid-based
327 reconstructions highlights that the two records show very different trajectories, since the
328 pollen-based reconstruction of this site shows a consistent warming trend throughout the
329 Holocene. Although Tarrats et al. (2018) argue that discrepancies between their temperature
330 reconstructions and pollen-based reconstructions reflects the fact that the vegetation of Iberia,
331 including the mountain areas, is largely driven by moisture changes and perhaps is not a good
332 indicator of temperature, we have shown that there is sufficient information in the pollen
333 records to reconstruct temperature and moisture independently (Table 2, Table S2). Thus, the
334 cause of the differences between the pollen-based and chironomid-based reconstructions at
335 Basa de la Mora is presumably related to methodology. In particular, the chironomid
336 reconstructions use a training data set that does not include samples from the Pyrenees, or
337 indeed the Mediterranean more generally, and may therefore not provide good analogues for
338 Holocene changes at this site.

339 The lack of a clear trend in MTWA in our reconstructions is not consistent with insolation
340 forcing, which shows a declining trend during the Holocene nor is it consistent with simulated
341 changes in MTWA in transient climate model simulations (see supplementary materials for
342 detailed description) of the summer temperature response to changing insolation forcing over
343 the ~~late~~ Holocene in this region (SI Fig. S9). The change in moisture gradient during the mid-
344 Holocene, however, suggests an alternative explanation whereby changes in summer
345 temperature are a response to land-surface feedbacks associated with changes in moisture.
346 Specifically, the observed increased advection of moisture into eastern Iberia would have
347 created wetter conditions there, which in turn would permit increased evapotranspiration,
348 implying less allocation of available net radiation to sensible heating, and resulting in cooler
349 air temperatures. ~~Specifically, the increased advection of moisture into eastern Iberia created~~

350 ~~wetter conditions leading to increased evapotranspiration, less allocation of available net~~
351 ~~radiation to sensible heating, and resulting in cooler air temperatures.~~ Our reconstructions show
352 that the west-east moisture gradient in mid-Holocene was significantly flatter than the steep
353 moisture gradient today, implying a significant increase in moisture advection into the
354 continental interior during this period. Mauri et al. (2015) also showed that summers were
355 generally wetter than present in the east but drier than present in the west at early to mid-
356 Holocene, supporting the idea of a flatter west-east gradient. ~~Stronger moisture advection is~~
357 ~~not a feature of the transient climate model simulations, which may explain why these~~
358 ~~simulations do not show a strong modification of the insolation-driven changes in summer~~
359 ~~temperature. The failure of the current generation of climate models to simulate the observed~~
360 ~~strengthening of moisture transport into Europe and Eurasia during the mid-Holocene has been~~
361 ~~noted by other studies (e.g. Bartlein et al., 2017; Mauri et al., 2014). This data-model mismatch~~
362 ~~highlights the need for better modelling of land-surface feedbacks on atmospheric circulation~~
363 ~~and moisture.~~

364 We have shown that stronger moisture advection is not a feature of transient climate model
365 simulations of the Holocene, which may explain why these simulations do not show a strong
366 modification of the insolation-driven changes in summer temperature (Fig. S9). Although the
367 amplitude differs, all of the models show a general decline in summer temperature. The failure
368 of the current generation of climate models to simulate the observed strengthening of moisture
369 transport into Europe and Eurasia during the mid-Holocene has been noted for previous
370 versions of these models (e.g. Bartlein et al., 2017; Mauri et al., 2014) and also shown in Fig.
371 S10. Mauri et al. (2014), for example, showed that climate models participating in the last
372 phase of the Coupled Model Intercomparison Project (CMIP5/PMIP3) were unable to
373 reproduce reconstructed climate patterns over Europe at 6000 yr B.P. and indicated that this
374 resulted from over-sensitivity to changes in insolation forcing and the failure to simulate
375 increased moisture transport into the continent. (Bartlein et al., (2017) showed that the
376 CMIP5/PMIP3 models simulated warmer and drier conditions in mid-continental Eurasia at
377 6000 yr B.P., inconsistent with palaeo-environmental reconstructions from the region, as a
378 result of the simulated reduction in the zonal temperature gradient which resulted in weaker
379 westerly flow and reduced moisture fluxes into the mid-continent. They also pointed out the
380 strong feedback between drier conditions and summer temperatures. The drying of the mid-
381 continent is also a strong feature of the mid-Holocene simulations made with the current
382 generation of CMIP6/PMIP4 models (Brierley et al., 2020). The persistence of these data-

383 model mismatches highlights the need for better modelling of land-surface feedbacks on
 384 atmospheric circulation and moisture.

385 Speleothem oxygen-isotope data from the Iberian Peninsula provide support for our pollen-
 386 based reconstructions of changes in the west-east gradient of moisture through the Holocene.
 387 The speleothem records show a progressive increase in temperature from the Younger Dryas
 388 onwards, although the trend is less marked in the west than the east (Baldini et al., 2019). This
 389 warming trend is consistent with our reconstructions of changes in MTCO through the
 390 Holocene. ~~However, S~~speleothem records also show distinctly different patterns in moisture
 391 availability, with sites in western Iberia indicating wetter environments during early Holocene
 392 and a transition to drier conditions from ca 7.5 cal ka BP to the present (Stoll et al., 2013;
 393 Thatcher et al., 2020) while eastern sites record wetter conditions persisting from 9 to 4 cal ka
 394 (Walczak et al., 2015). This finding would support the weaker west to east moisture gradient
 395 shown by our results.

396 Pollen data are widely used for the quantitative reconstruction of past climates (see discussion
 397 in Bartlein et al., 2011). Nevertheless, climate is not the only driver of vegetation changes. On
 398 glacial-interglacial timescales, changes in CO₂ have a direct impact on plant physiological
 399 processes and reductions in plant water-use efficiency at low CO₂ result in vegetation
 400 appearing to reflect drier conditions than ~~w~~ were experienced in reality (Farquhar, 1997; Gerhart
 401 and Ward, 2010; Prentice et al., 2017; Prentice and Harrison, 2009). The difference between
 402 post- and pre-industrial CO₂ levels could also influence the reliability of moisture
 403 reconstructions based on modern training data sets. ~~We have not accounted for the impact of~~
 404 ~~changing CO₂ in our reconstructions of α , although there are techniques to do this (Prentice et~~
 405 ~~al., 2011, 2017; Wei et al., 2021).~~ However, the change in CO₂ over the Holocene was only 40
 406 ppm. ~~Prentice et al. (2021)~~ (Prentice et al., (2022)) shows that this change relative to modern
 407 levels has only a small impact on pollen-based reconstructed moisture indices. The magnitude
 408 of this impact is within the uncertainties on our reconstructions. Furthermore, accounting for
 409 the effect of this change in CO₂ ~~or would~~ not won't affect the reconstructed west-east gradient
 410 through time. Therefore, w~~We have not accounted for the impact of changing CO₂ in our~~
 411 ~~reconstructions of α , although there are techniques to do this (Prentice et al., 2011, 2017; Wei~~
 412 ~~et al., 2021).~~ A more serious issue for our reconstructions may be the extent to which the
 413 vegetation cover of Iberia was substantially modified by human activities during the Holocene.
 414 While there is no doubt that anthropogenic activities were important at the local scale and

415 particularly in the later Holocene (e.g. Abel-Schaad and López-Sáez, 2013; Connor et al., 2019;
416 Fyfe et al., 2019; Mighall et al., 2006; Revelles et al., 2015), most of the sites used for our
417 reconstructions are not associated with archaeological evidence of agriculture or substantial
418 landscape modification. Furthermore, the consistency of the reconstructed changes in climate
419 across sites provides support for these being largely a reflection of regional climate changes.

420 We have used a modified version of fxTWA-PLS to reconstruct Holocene climates of the
421 Iberian Peninsula because this modification reduced the compression bias in MTCO and
422 MTWA, and specifically reduces the maximum bias in MTCO, MTWA and α . Although this
423 modified approach produces better overall reconstructions (Appendix A), its use does not
424 change the reconstructed trends in these variables through time (SI Fig. S12[†]). Thus, the
425 finding that winter temperatures are a direct reflection of insolation forcing whereas summer
426 temperatures are influenced by land-surface feedbacks and changes in atmospheric circulation
427 is robust to the method used. However, while we use a much larger data set than previous
428 reconstructions, the distribution of pollen sites is uneven and the northern part of the Peninsula
429 is better sampled than the southwest, which could lead to some uncertainties in the
430 interpretation of changes in the west-east gradient of moisture. It would, therefore, be useful to
431 specifically target the southwestern part of the Iberian Peninsula for new data collection.
432 Alternatively, it would be useful to apply the approach used here to the whole of Eurasia, given
433 that the failure of state-of-the-art climate models to advect moisture into the continental interior
434 appears to be a feature of the whole region (Bartlein et al., 2017) and not the Peninsula alone.

435 **5. Conclusion**

436 We have used a pollen data set representing 117 sites across the Iberian Peninsula to make
437 quantitative reconstructions of summer and winter temperature and an index of annual moisture
438 through the Holocene. We show that the trends in winter temperature broadly follow the
439 changes orbital forcing. Summer temperatures, however, do not follow the changes in orbital
440 forcing but appear to be influenced by land-surface feedbacks associated with changes in
441 moisture. The west-east gradient in moisture was considerably less pronounced during the mid-
442 Holocene (8-4 ka).

443

444 **Data and Code Availability**

445 All the data used are public access and cited here. The code used to generate the climate
446 reconstructions is available at <https://github.com/ml4418/Iberia-paper.git>.

447 **Supplement.** The supplement related to this article is available online.

448 **Competing interests.** We declare that we have no conflict of interest.

449 **Author Contributions.** ML, ICP and SPH designed the study. ML, ICP and CJFtB designed
450 the modifications to fxTWA-PLS. PG-S and GG-R provided pollen data and insights into the
451 regional palaeoclimate histories. ML carried out the analyses. ML and SPH wrote the first
452 draft of the paper and all authors contributed to the final draft.

453 **Acknowledgements.** ML acknowledges support from Imperial College through the Lee
454 Family Scholarship. YS and SPH acknowledge support from the ERC-funded project GC 2.0
455 (Global Change 2.0: Unlocking the past for a clearer future; grant number 694481). ICP
456 acknowledges support from the ERC under the European Union Horizon 2020 research and
457 innovation programme (grant agreement no: 787203 REALM). This work is a contribution to
458 the project "Origen y Cuantificación de los Cambios Paleoambientales en el Pirineo:
459 Variabilidad climática e impacto humano" (PYCACHU: PID2019-106050RB-I00)" funded by
460 the Ministerio de Ciencia e Innovación.

461 **Financial support.** This research has been supported by Lee Family Scholarship fund, and
462 the European Research Council (grant no. GC2.0, 694481, and grant no. REALM, 787203).

463 **References**

- 464 Abel-Schaad, D., López-Sáez, J.A.: Vegetation changes in relation to fire history and human
 465 activities at the Peña Negra mire (Bejar Range, Iberian Central Mountain System, Spain)
 466 during the past 4,000 years. *Veg. Hist. Archaeobot.* 22, 199–214.
 467 <https://doi.org/10.1007/s00334-012-0368-9>, 2013.
- 468 Abel-Schaad, D. and López-Sáez, J. A.: Vegetation changes in relation to fire history and
 469 human activities at the Peña Negra mire (Bejar Range, Iberian Central Mountain System,
 470 Spain) during the past 4,000 years, *Veg. Hist. Archaeobot.*, 22, 199–214,
 471 [doi:10.1007/s00334-012-0368-9](https://doi.org/10.1007/s00334-012-0368-9), 2013.
- 472 Andrade, C., Contente, J. and Santos, J. A.: Climate change projections of aridity conditions
 473 in the Iberian Peninsula, *Water*, 13(15), [doi:10.3390/w13152035](https://doi.org/10.3390/w13152035), 2021a.
- 474 Andrade, C., Contente, J. and Santos, J. A.: Climate change projections of dry and wet events
 475 in Iberia based on the WASP-Index, *Climate*, 9(6), [doi:10.3390/cli9060094](https://doi.org/10.3390/cli9060094), 2021b.
- 476 Aranbarri, J., Gonzalez Samperiz, P., Valero-Garcés, B., Moreno, A., Gil-Romera, G.,
 477 Sevilla-Callejo, M., Garcia-Prieto, E., Di Rita, F., Mata, M. del Pi., Morellón, M., Magri, D.,
 478 Rodriguez-Lazaro, J. and Carrión, J.: Rapid climatic changes and resilient vegetation during
 479 the Lateglacial and Holocene in a continental region of south-western Europe, *Glob. Planet.*
 480 *Change*, 114, 50–65, [doi:10.1016/j.gloplacha.2014.01.003](https://doi.org/10.1016/j.gloplacha.2014.01.003), 2014.
- 481 Aranbarri, J., González-Sampériz, P., Iriarte, E., Moreno, A., Rojo-Guerra, M., Peña-
 482 Chocarro, L., Valero-Garcés, B., Leunda, M., García-Prieto, E., Sevilla-Callejo, M., Gil-
 483 Romera, G., Magri, D. and Rodríguez-Lázaro, J.: Human–landscape interactions in the
 484 Conquezueta–Ambrona Valley (Soria, continental Iberia): From the early Neolithic land use
 485 to the origin of the current oak woodland, *Palaeogeogr. Palaeoclimatol. Palaeoecol.*, 436, 41–
 486 57, [doi:https://doi.org/10.1016/j.palaeo.2015.06.030](https://doi.org/10.1016/j.palaeo.2015.06.030), 2015.
- 487 Baldini, L. M., Baldini, J. U. L., McDermott, F., Arias, P., Cueto, M., Fairchild, I. J.,
 488 Hoffmann, D. L., Matthey, D. P., Müller, W., Nita, D. C., Ontañón, R., Garcíá-Moncó, C. and
 489 Richards, D. A.: North Iberian temperature and rainfall seasonality over the Younger Dryas
 490 and Holocene, *Quat. Sci. Rev.*, 226, 105998,
 491 [doi:https://doi.org/10.1016/j.quascirev.2019.105998](https://doi.org/10.1016/j.quascirev.2019.105998), 2019.
- 492 Bartlein, P. J., Prentice, I. C. and Webb, T.: Climatic response surfaces from pollen data for
 493 some Eastern North American taxa, *J. Biogeogr.*, 13(1), 35, [doi:10.2307/2844848](https://doi.org/10.2307/2844848), 1986.
- 494 Bartlein, P. J., Harrison, S. P., Brewer, S., Connor, S., Davis, B. A. S., Gajewski, K., Guiot,
 495 J., Harrison-Prentice, T. I., Henderson, A., Peyron, O., Prentice, I. C., Scholze, M., Seppä, H.,
 496 Shuman, B., Sugita, S., Thompson, R. S., Vial, A. E., Williams, J. and Wu, H.: Pollen-based
 497 continental climate reconstructions at 6 and 21 ka: A global synthesis, *Clim. Dyn.*, 37(3),
 498 775–802, [doi:10.1007/s00382-010-0904-1](https://doi.org/10.1007/s00382-010-0904-1), 2011.
- 499 Bartlein, P. J., Harrison, S. P. and Izumi, K.: Underlying causes of Eurasian midcontinental

- 500 aridity in simulations of mid-Holocene climate, *Geophys. Res. Lett.*, 44(17), 9020–9028,
501 doi:10.1002/2017GL074476, 2017.
- 502 Blaauw, M. and Christeny, J. A.: Flexible paleoclimate age-depth models using an
503 autoregressive gamma process, *Bayesian Anal.*, 6(3), 457–474, doi:10.1214/11-BA618, 2011.
- 504 Blaauw, M., Christen, J. A., Lopez, M. A. A. V., V., J. E. O. M. G., Belding, T., Theiler, J.,
505 Gough, B. and Karney, C.: rbacon: Age-depth modelling using Bayesian statistics, [online]
506 Available from: <https://cran.r-project.org/package=rbacon>, 2021.
- 507 ter Braak, C. J. F. and Juggins, S.: Weighted averaging partial least squares regression (WA-
508 PLS): An improved method for reconstructing environmental variables from species
509 assemblages, *Hydrobiologia*, 269(1), 485–502, doi:10.1007/BF00028046, 1993.
- 510 Brierley, C. M., Zhao, A., Harrison, S. P., Braconnot, P., Williams, C. J. R., Thornalley, D. J.
511 R., Shi, X., Peterschmitt, J.-Y., Ohgaito, R., Kaufman, D. S., Kageyama, M., Hargreaves, J.
512 C., Erb, M. P., Emile-Geay, J., D’Agostino, R., Chandan, D., Carré, M., Bartlein, P., Zheng,
513 W., Zhang, Z., Zhang, Q., Yang, H., Volodin, E. M., Tomas, R. A., Routson, C., Peltier, W.
514 R., Otto-Bliesner, B., Morozova, P. A., McKay, N. P., Lohmann, G., Legrande, A. N., Guo,
515 C., Cao, J., Brady, E., Annan, J. D. and Abe-Ouchi, A.: Large-scale features and evaluation
516 of the PMIP4-CMIP6 midHolocene simulations, *Clim. Past Discuss.*, 2020, 1–35,
517 doi:10.5194/cp-2019-168, 2020.
- 518 Carrión, J. S., Fernández, S., González-Sampériz, P., Gil-Romera, G., Badal, E., Carrión-
519 Marco, Y., López-Merino, L., López-Sáez, J. A., Fierro, E. and Burjachs, F.: Expected trends
520 and surprises in the Lateglacial and Holocene vegetation history of the Iberian Peninsula and
521 Balearic Islands, *Rev. Palaeobot. Palynol.*, 162(3), 458–475,
522 doi:<https://doi.org/10.1016/j.revpalbo.2009.12.007>, 2010.
- 523 Carrión, Y., Kaal, J., López-Sáez, J. A., López-Merino, L. and Martínez Cortizas, A.:
524 Holocene vegetation changes in NW Iberia revealed by anthracological and palynological
525 records from a colluvial soil, *The Holocene*, 20(1), 53–66, doi:10.1177/0959683609348849,
526 2009.
- 527 Carvalho, D., Pereira, S. and Rocha, A.: Future surface temperature changes for the Iberian
528 Peninsula according to EURO-CORDEX climate projections, *Clim. Dyn.*, 56, 1–16,
529 doi:10.1007/s00382-020-05472-3, 2021.
- 530 Cheddadi, R., Yu, G., Joel, G., Harrison, S., Prentice, I. and Colin, I.: The climate of Europe
531 6000 years ago, *cd*, 13, 1, doi:10.1007/s003820050148, 1997.
- 532 Chevalier, M., Davis, B. A. S., Heiri, O., Seppä, H., Chase, B. M., Gajewski, K., Lacourse,
533 T., Telford, R. J., Finsinger, W., Guiot, J., Kühl, N., Maezumi, S. Y., Tipton, J. R., Carter, V.
534 A., Brussel, T., Phelps, L. N., Dawson, A., Zanon, M., Vallé, F., Nolan, C., Mauri, A., de
535 Vernal, A., Izumi, K., Holmström, L., Marsicek, J., Goring, S., Sommer, P. S., Chaput, M.
536 and Kupriyanov, D.: Pollen-based climate reconstruction techniques for late Quaternary
537 studies, *Earth-Science Rev.*, 210, 103384,

- 538 doi:<https://doi.org/10.1016/j.earscirev.2020.103384>, 2020.
- 539 Connor, S., Vanni re, B., Colombaroli, D., Anderson, R., Carri n, J., Ejarque, A., Gil-
540 Romera, G., Gonzalez Samperiz, P., H fer, D., Morales-Molino, C., Revelles, J., Schneider,
541 H., Knaap, W., Leeuwen, J. and Woodbridge, J.: Humans take control of fire-driven diversity
542 changes in Mediterranean Iberia’s vegetation during the mid–late Holocene, *The Holocene*,
543 29, 095968361982665, doi:10.1177/0959683619826652, 2019.
- 544 Davis, T. W., Prentice, I. C., Stocker, B. D., Thomas, R. T., Whitley, R. J., Wang, H., Evans,
545 B. J., Gallego-Sala, A. V., Sykes, M. T. and Cramer, W.: Simple process-led algorithms for
546 simulating habitats (SPLASH v.1.0): Robust indices of radiation, evapotranspiration and
547 plant-available moisture, *Geosci. Model Dev.*, 10(2), 689–708, doi:10.5194/gmd-10-689-
548 2017, 2017.
- 549 Eilers, P. H. and Marx, B. D.: *Practical smoothing: The Joys of P-splines*, edited by P. H.
550 Eilers and B. D. Marx, Cambridge University Press., 2021.
- 551 Farquhar, G. D.: Carbon dioxide and vegetation, *Science* (80-.), 278(5342), 1411,
552 doi:10.1126/science.278.5342.1411, 1997.
- 553 Fyfe, R. M., Woodbridge, J., Palmisano, A., Bevan, A., Shennan, S., Burjachs, F., Legarra
554 Herrero, B., Garc a Puchol, O., Carri n, J. S., Revelles, J. and Roberts, C. N.: Prehistoric
555 palaeodemographics and regional land cover change in eastern Iberia, *Holocene*, 29(5), 799–
556 815, doi:10.1177/0959683619826643, 2019.
- 557 Gerhart, L. M. and Ward, J. K.: Plant responses to low [CO₂] of the past, *New Phytol.*,
558 188(3), 674–695, doi:<https://doi.org/10.1111/j.1469-8137.2010.03441.x>, 2010.
- 559 Gonz lez-Samp riz, P., Aranbarri, J., P rez-Sanz, A., Gil-Romera, G., Moreno, A., Leunda,
560 M., Sevilla-Callejo, M., Corella, J. P., Morell n, M., Oliva, B. and Valero-Garc s, B.:
561 Environmental and climate change in the southern Central Pyrenees since the Last Glacial
562 Maximum: A view from the lake records, *Catena*, 149, 668–688,
563 doi:<https://doi.org/10.1016/j.catena.2016.07.041>, 2017.
- 564 Granados, I. and Toro, M.: Recent warming in a high mountain lake (Laguna Cimera, Central
565 Spain) inferred by means of fossil chironomids, *J. Limnol.*, 59 (suppl., 109–119,
566 doi:10.4081/jlimnol.2000.s1.109, 2000.
- 567 Harrison, S., Shen, Y. and Sweeney, L.: Pollen data and charcoal data of the Iberian
568 Peninsula (version 3), [online] Available from: <https://doi.org/10.17864/1947.000369>, 2022.
- 569 Harrison, S. P.: Modern pollen data for climate reconstructions, version 1 (SMPDS), ,
570 doi:<http://dx.doi.org/10.17864/1947.194>, 2019.
- 571 Holden, P. B., Birks, H. J. B., Brooks, S. J., Bush, M. B., Hwang, G. M., Matthews-Bird, F.,
572 Valencia, B. G. and van Woesik, R.: BUMPER v1.0: a Bayesian user-friendly model for
573 palaeo-environmental reconstruction, *Geosci. Model Dev.*, 10(1), 483–498,

- 574 doi:10.5194/gmd-10-483-2017, 2017.
- 575 Kaufman, D., McKay, N., Routson, C., Erb, M., Davis, B., Heiri, O., Jaccard, S., Tierney, J.,
 576 Dätwyler, C., Axford, Y., Brussel, T., Cartapanis, O., Chase, B., Dawson, A., de Vernal, A.,
 577 Engels, S., Jonkers, L., Marsicek, J., Moffa-Sánchez, P., Morrill, C., Orsi, A., Rehfeld, K.,
 578 Saunders, K., Sommer, P. S., Thomas, E., Tonello, M., Tóth, M., Vachula, R., Andreev, A.,
 579 Bertrand, S., Biskaborn, B., Bringué, M., Brooks, S., Caniupán, M., Chevalier, M., Cwynar,
 580 L., Emile-Geay, J., Fegyveresi, J., Feurdean, A., Finsinger, W., Fortin, M.-C., Foster, L., Fox,
 581 M., Gajewski, K., Grosjean, M., Hausmann, S., Heinrichs, M., Holmes, N., Ilyashuk, B.,
 582 Ilyashuk, E., Juggins, S., Khider, D., Koinig, K., Langdon, P., Larocque-Tobler, I., Li, J.,
 583 Lotter, A., Luoto, T., Mackay, A., Magyari, E., Malevich, S., Mark, B., Massaferró, J.,
 584 Montade, V., Nazarova, L., Novenko, E., Pařil, P., Pearson, E., Peros, M., Pienitz, R.,
 585 Płóciennik, M., Porinchu, D., Potito, A., Rees, A., Reinemann, S., Roberts, S., Rolland, N.,
 586 Salonen, S., Self, A., Seppä, H., Shala, S., St-Jacques, J.-M., Stenni, B., Syrykh, L., Tarrats,
 587 P., Taylor, K., van den Bos, V., Velle, G., Wahl, E., Walker, I., Wilmshurst, J., Zhang, E. and
 588 Zhilich, S.: A global database of Holocene paleotemperature records, *Sci. Data*, 7(1), 115,
 589 doi:10.1038/s41597-020-0445-3, 2020.
- 590 Liu, M., Prentice, I. C., ter Braak, C. J. F. and Harrison, S. P.: An improved statistical
 591 approach for reconstructing past climates from biotic assemblages, *Proc. R. Soc. A Math.*,
 592 476(2243), doi:https://doi.org/10.1098/rspa.2020.0346, 2020.
- 593 Martínez-Cortizas, A., Costa-Casais, M. and López-Sáez, J. A.: Environmental change in
 594 NW Iberia between 7000 and 500cal BC, *Quat. Int.*, 200(1), 77–89,
 595 doi:https://doi.org/10.1016/j.quaint.2008.07.012, 2009.
- 596 Mauri, A., Davis, B. A. S., Collins, P. M. and Kaplan, J. O.: The influence of atmospheric
 597 circulation on the mid-Holocene climate of Europe: a data–model comparison, *Clim. Past*,
 598 10(5), 1925–1938, doi:10.5194/cp-10-1925-2014, 2014.
- 599 Mauri, A., Davis, B. A. S., Collins, P. M. and Kaplan, J. O.: The climate of Europe during the
 600 Holocene: A gridded pollen-based reconstruction and its multi-proxy evaluation, *Quat. Sci.*
 601 *Rev.*, 112, 109–127, doi:10.1016/j.quascirev.2015.01.013, 2015.
- 602 Mighall, T. M., Martínez Cortizas, A., Biester, H. and Turner, S. E.: Proxy climate and
 603 vegetation changes during the last five millennia in NW Iberia: Pollen and non-pollen
 604 palynomorph data from two ombrotrophic peat bogs in the North Western Iberian Peninsula,
 605 *Rev. Palaeobot. Palynol.*, 141(1–2), 203–223, doi:10.1016/j.revpalbo.2006.03.013, 2006.
- 606 Millet, L., Rius, D., Galop, D., Heiri, O. and Brooks, S. J.: Chironomid-based reconstruction
 607 of Lateglacial summer temperatures from the Ech palaeolake record (French western
 608 Pyrenees), *Palaeogeogr. Palaeoclimatol. Palaeoecol.*, 315–316, 86–99,
 609 doi:https://doi.org/10.1016/j.palaeo.2011.11.014, 2012.
- 610 Morellón, M., Aranbarri, J., Moreno, A., González-Sampériz, P. and Valero-Garcés, B. L.:
 611 Early Holocene humidity patterns in the Iberian Peninsula reconstructed from lake, pollen
 612 and speleothem records, *Quat. Sci. Rev.*, 181, 1–18,
 613 doi:https://doi.org/10.1016/j.quascirev.2017.11.016, 2018.

- 614 Muñoz Sobrino, C., Heiri, O., Hazekamp, M., van der Velden, D., Kirilova, E. P., García-
615 Moreiras, I. and Lotter, A. F.: New data on the Lateglacial period of SW Europe: a high
616 resolution multiproxy record from Laguna de la Roya (NW Iberia), *Quat. Sci. Rev.*, 80, 58–
617 77, doi:<https://doi.org/10.1016/j.quascirev.2013.08.016>, 2013.
- 618 New, M., Lister, D. and Hulme, M.: A high-resolution data set of surface climate over global
619 land areas, *Clim. Res.*, 21(1), 1–25 [online] Available from: [http://www.int-](http://www.int-res.com/abstracts/cr/v21/n1/p1-25/)
620 [res.com/abstracts/cr/v21/n1/p1-25/](http://www.int-res.com/abstracts/cr/v21/n1/p1-25/), 2002.
- 621 Overpeck, J. T., Webb, T. and Prentice, I. C.: Quantitative interpretation of fossil pollen
622 spectra: Dissimilarity coefficients and the method of modern analogs, *Quat. Res.*, 23(1), 87–
623 108, doi:[10.1016/0033-5894\(85\)90074-2](https://doi.org/10.1016/0033-5894(85)90074-2), 1985.
- 624 Peyron, O., Guiot, J., Cheddadi, R., Tarasov, P., Reille, M., de Beaulieu, J.-L., Bottema, S.
625 and Andrieu, V.: Climatic reconstruction in Europe for 18,000 yr B.P. from pollen data, *Quat.*
626 *Res.*, 49(2), 183–196, doi:<https://doi.org/10.1006/qres.1997.1961>, 1998.
- 627 Prentice, I. C. and Harrison, S. P.: Ecosystem effects of CO₂ concentration: evidence from
628 past climates, *Clim. Past*, 5(3), 297–307, doi:[10.5194/cp-5-297-2009](https://doi.org/10.5194/cp-5-297-2009), 2009.
- 629 Prentice, I. C., Meng, T., Wang, H., Harrison, S. P., Ni, J. and Wang, G.: Evidence of a
630 universal scaling relationship for leaf CO₂ drawdown along an aridity gradient, *New Phytol.*,
631 190(1), 169–180, doi:<https://doi.org/10.1111/j.1469-8137.2010.03579.x>, 2011.
- 632 Prentice, I. C., Cleator, S. F., Huang, Y. H., Harrison, S. P. and Roulstone, I.: Reconstructing
633 ice-age palaeoclimates: Quantifying low-CO₂ effects on plants, *Glob. Planet. Change*, 149,
634 166–176, doi:<https://doi.org/10.1016/j.gloplacha.2016.12.012>, 2017.
- 635 Prentice, I. C., Villegas-Diaz, R. and Harrison, S. P.: Accounting for atmospheric carbon
636 dioxide variations in pollen-based reconstruction of past hydroclimates, *Glob. Planet.*
637 *Change*, 2022.
- 638 Reimer, P. J., Austin, W. E. N., Bard, E., Bayliss, A., Blackwell, P. G., Bronk Ramsey, C.,
639 Butzin, M., Cheng, H., Edwards, R. L., Friedrich, M., Grootes, P. M., Guilderson, T. P.,
640 Hajdas, I., Heaton, T. J., Hogg, A. G., Hughen, K. A., Kromer, B., Manning, S. W.,
641 Muscheler, R., Palmer, J. G., Pearson, C., Van Der Plicht, J., Reimer, R. W., Richards, D. A.,
642 Scott, E. M., Southon, J. R., Turney, C. S. M., Wacker, L., Adolphi, F., Büntgen, U., Capano,
643 M., Fahrni, S. M., Fogtmann-Schulz, A., Friedrich, R., Köhler, P., Kudsk, S., Miyake, F.,
644 Olsen, J., Reinig, F., Sakamoto, M., Sookdeo, A. and Talamo, S.: The IntCal20 Northern
645 Hemisphere radiocarbon age calibration curve (0–55 cal kBP), *Radiocarbon*, 62(4), 725–757,
646 doi:[10.1017/RDC.2020.41](https://doi.org/10.1017/RDC.2020.41), 2020.
- 647 Revelles, J., Cho, S., Iriarte, E., Burjachs, F., van Geel, B., Palomo, A., Piqué, R., Peña-
648 Chocarro, L. and Terradas, X.: Mid-Holocene vegetation history and Neolithic land-use in
649 the Lake Banyoles area (Girona, Spain), *Palaeogeogr. Palaeoclimatol. Palaeoecol.*, 435, 70–
650 85, doi:[10.1016/j.palaeo.2015.06.002](https://doi.org/10.1016/j.palaeo.2015.06.002), 2015.

- 651 Salonen, J. S., Ilvonen, L., Seppä, H., Holmström, L., Telford, R. J., Gaidamavičius, A.,
652 Stančikaitė, M. and Subetto, D.: Comparing different calibration methods (WA/WA-PLS
653 regression and Bayesian modelling) and different-sized calibration sets in pollen-based
654 quantitative climate reconstruction, *The Holocene*, 22(4), 413–424,
655 doi:10.1177/0959683611425548, 2011.
- 656 Shen, Y., Sweeney, L., Liu, M., Lopez Saez, J. A., Pérez-Díaz, S., Luelmo-Lautenschlaeger,
657 R., Gil-Romera, G., Hoefler, D., Jiménez-Moreno, G., Schneider, H., Prentice, I. C. and
658 Harrison, S. P.: Reconstructing burnt area during the Holocene: an Iberian case study, *Clim.
659 Past Discuss.*, 2021, 1–23, doi:10.5194/cp-2021-36, 2021.
- 660 Stoll, H. M., Moreno, A., Mendez-Vicente, A., Gonzalez-Lemos, S., Jimenez-Sanchez, M.,
661 Dominguez-Cuesta, M. J., Edwards, R. L., Cheng, H. and Wang, X.: Paleoclimate and
662 growth rates of speleothems in the northwestern Iberian Peninsula over the last two glacial
663 cycles, *Quat. Res.*, 80, 284–290, doi:10.1016/j.yqres.2013.05.002, 2013.
- 664 Tarrats, P., Heiri, O., Valero-Garcés, B., Cañedo-Argüelles, M., Prat, N., Rieradevall, M. and
665 González-Sampériz, P.: Chironomid-inferred Holocene temperature reconstruction in Basa de
666 la Mora Lake (Central Pyrenees), *The Holocene*, 28(11), 1685–1696,
667 doi:10.1177/0959683618788662, 2018.
- 668 Tarroso, P., Carrión, J., Dorado-Valiño, M., Queiroz, P., Santos, L., Valdeolmillos-
669 Rodríguez, A., Célio Alves, P., Brito, J. C. and Cheddadi, R.: Spatial climate dynamics in the
670 Iberian Peninsula since 15 000 yr BP, *Clim. Past*, 12(5), 1137–1149, doi:10.5194/cp-12-
671 1137-2016, 2016.
- 672 Thatcher, D. L., Wanamaker, A. D., Denniston, R. F., Asmerom, Y., Polyak, V. J., Fullick,
673 D., Ummenhofer, C. C., Gillikin, D. P. and Haws, J. A.: Hydroclimate variability from
674 western Iberia (Portugal) during the Holocene: Insights from a composite stalagmite isotope
675 record, *The Holocene*, 30(7), 966–981, doi:https://doi.org/10.1177/0959683620908648,
676 2020.
- 677 Villegas-Diaz, Roberto; Cruz-Silva, Esmeralda; Harrison, S. P.: ageR: Supervised age
678 models, , doi:10.5281/zenodo.4636715, 2021.
- 679 Walczak, I. W., Baldini, J. U. L., Baldini, L. M., McDermott, F., Marsden, S., Standish, C.
680 D., Richards, D. A., Andreo, B. and Slater, J.: Reconstructing high-resolution climate using
681 CT scanning of unsectioned stalagmites: A case study identifying the mid-Holocene onset of
682 the Mediterranean climate in southern Iberia, *Quat. Sci. Rev.*, 127, 117–128,
683 doi:https://doi.org/10.1016/j.quascirev.2015.06.013, 2015.
- 684 Wei, D., González-Sampériz, P., Gil-Romera, G., Harrison, S. P. and Prentice, I. C.: Seasonal
685 temperature and moisture changes in interior semi-arid Spain from the last interglacial to the
686 Late Holocene, *Quat. Res.*, 101, 143–155, doi:DOI: 10.1017/qua.2020.108, 2021.
- 687 Wu, H., Guiot, J., Brewer, S. and Guo, Z.: Climatic changes in Eurasia and Africa at the last
688 glacial maximum and mid-Holocene: reconstruction from pollen data using inverse

689 vegetation modelling, *Clim. Dyn.*, 29(2), 211–229, doi:10.1007/s00382-007-0231-3, 2007.

690

691 **Figure and Table Captions**

692 Figure 1. Climate space represented by mean temperature of the coldest month (MTCO),
 693 mean temperature of the warmest month (MTWA), and plant-available moisture as
 694 represented by α , an estimate of the ratio of actual evapotranspiration to equilibrium
 695 evapotranspiration. The grey points show climate values for a rectangular area (21° W ~ 150°
 696 E, 29° N ~ 82° N) enclosing the SMPDS data set, derived from the Climate Research Unit
 697 CRU CL 2.0 database (New et al., 2002). The black points show climate values of the
 698 SMPDS dataset. The red points show climate values of the Iberian Peninsula region in the
 699 SMPDS dataset.

700 Figure 24. Map showing the location of the 117 fossil sites in the Iberian Peninsula used for
 701 climate reconstructions. Sites lower than 1000 m above sea level are shown as squares, sites
 702 higher than 1000 m above sea level are shown as triangles. The base maps show modern (a)
 703 mean temperature of the coldest month (MTCO), (b) mean temperature of the warmest month
 704 (MTWA), and (c) plant-available moisture as represented by α , an estimate of the ratio of
 705 actual evapotranspiration to equilibrium evapotranspiration.

706 Figure 32. Reconstructed anomalies in climate at individual sites through time. The sites are
 707 grouped into high (>1000m) and low (<1000m) elevation sites and organised from west to east.
 708 Grey cells indicate periods or longitudes with no data. The individual plots show the anomalies
 709 in reconstructed (a,d) mean temperature of the coldest month (MTCO), (b,e) mean temperature
 710 of the warmest month (MTWA), and (c,f) plant-available moisture as represented by α , an
 711 estimate of the ratio of actual evapotranspiration to equilibrium evapotranspiration. The
 712 anomalies are expressed as deviations of the mean value in each bin (± 500 years) from the
 713 value at 0.5 ka at each site.

714 Figure 43. Reconstructed composite changes (anomalies to 0.5 ka) in (a) mean temperature of
 715 the coldest month (MTCO), (b) mean temperature of the warmest month (MTWA) and (c)
 716 plant-available moisture as represented by α , through the Holocene compared to changes in
 717 (d) winter and (e) summer insolation for the latitude of the Iberian Peninsula, using ± 500
 718 years as the bin. The black lines show mean values across sites, with vertical line segments
 719 showing the standard deviations of mean values using 1000 bootstrap cycles of site
 720 resampling.

721 Figure 54. Changes in the west-east gradient of plant-available moisture as represented by
 722 anomalies in α relative to 0.5 ka at individual sites through the Holocene. The red lines show
 723 the regression lines. The shades indicate the 95 % confidence intervals of the regression lines

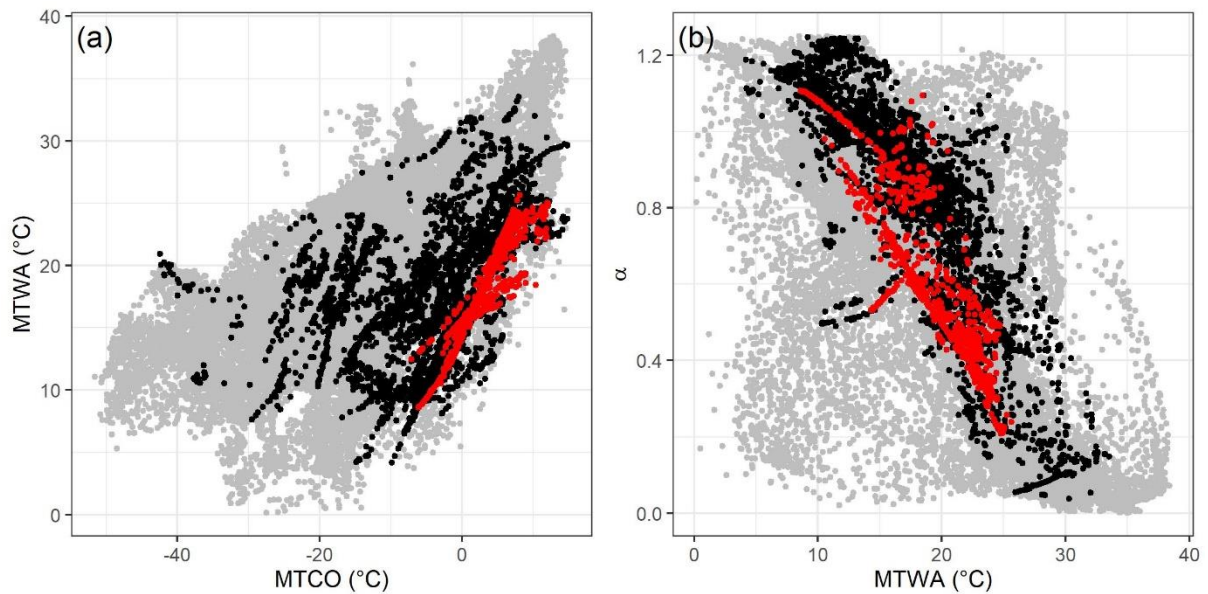
724 Figure 65. The relationship between mean temperature of the warmest month (MTWA) and
 725 plant-available moisture as represented by α (a) in the modern climate data set, and (b) in the
 726 Holocene reconstructions.

727 Table 1. Leave-out cross-validation (with geographically and climatically close sites
 728 removed) fitness of the modified version of fxTWA-PLS, for mean temperature of the coldest
 729 month (MTCO), mean temperature of the warmest month (MTWA) and plant-available
 730 moisture (α), with p-spline smoothed fx estimation, using bins of 0.02, 0.02 and 0.002,
 731 showing results for all the components. RMSEP is the root-mean-square error of prediction.
 732 Δ RMSEP is the per cent change of RMSEP using the current number of components than
 733 using one component less. p assesses whether using the current number of components is
 734 significantly different from using one component less, which is used to choose the last
 735 significant number of components (indicated in bold) to avoid over-fitting. The degree of
 736 overall compression is assessed by linear regression of the cross-validated reconstructions
 737 onto the climate variable, b_1 , $b_1.se$ are the slope and the standard error of the slope,
 738 respectively. The closer the slope (b_1) is to 1, the less the overall compression is.

739 Table 2. Canonical Correspondence Analysis (CCA) result of modern and fossil-
 740 reconstructed MTCO, MTWA and α . The summary statistics for the ANOVA-like
 741 permutation test (999 permutations) are also shown. VIF is the variance inflation factor, Df is
 742 the number of degrees of freedom, χ^2 is the constrained eigenvalue (or the sum of
 743 constrained eigenvalues for the whole model)-, F is significance, and Pr ($>F$) is the
 744 probability.

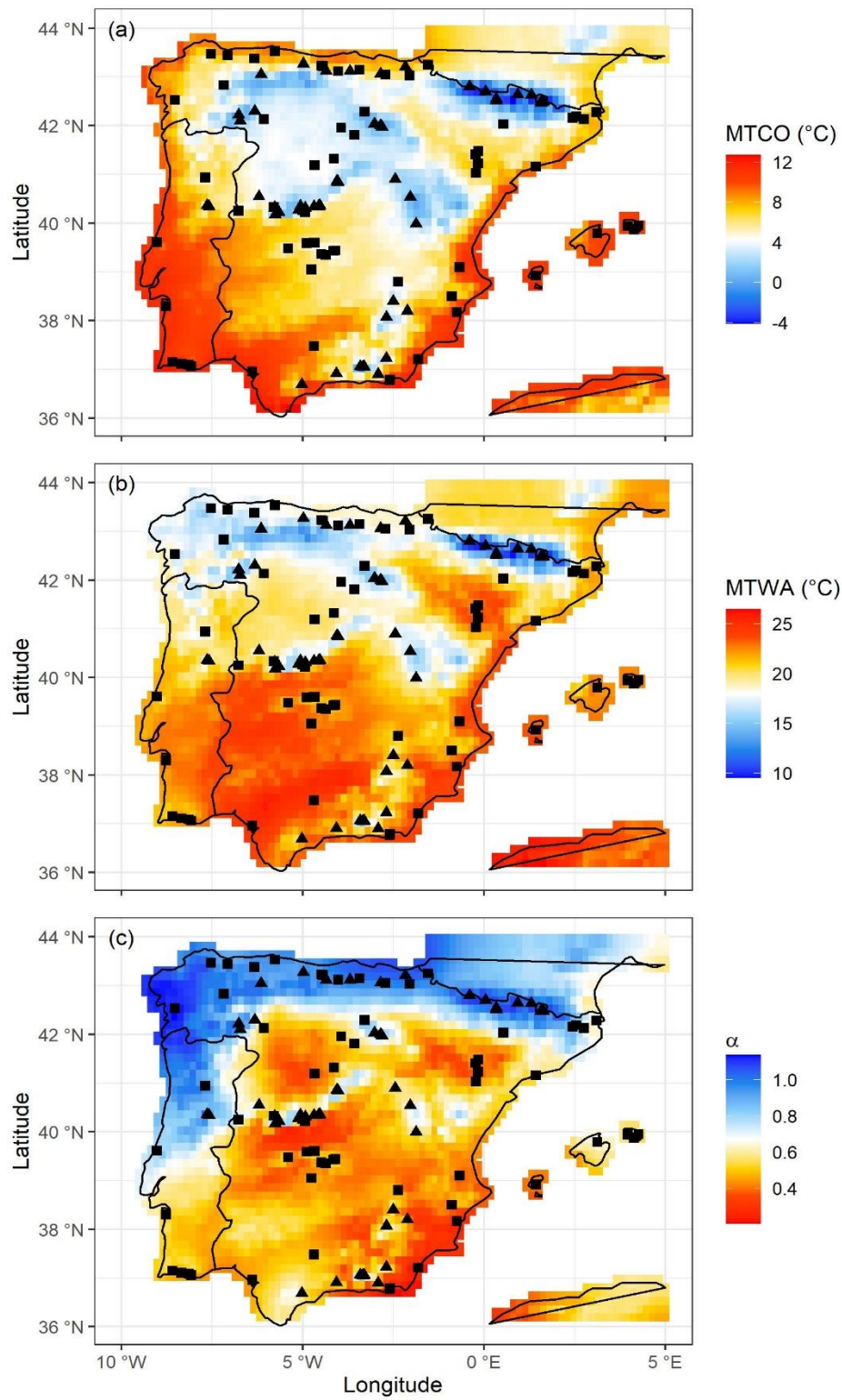
745 Table 3. Assessment of the significance of anomalies to 0.5 ka through time with latitude and
 746 elevation. The slope is obtained by linear regression of the anomaly onto the longitude or
 747 elevation. p is the significance of the slope (bold parts: $p < 0.05$). x_0 is the point where the
 748 anomaly is 0 in the linear equation, which indicates longitude or elevation where the anomaly
 749 changes sign.

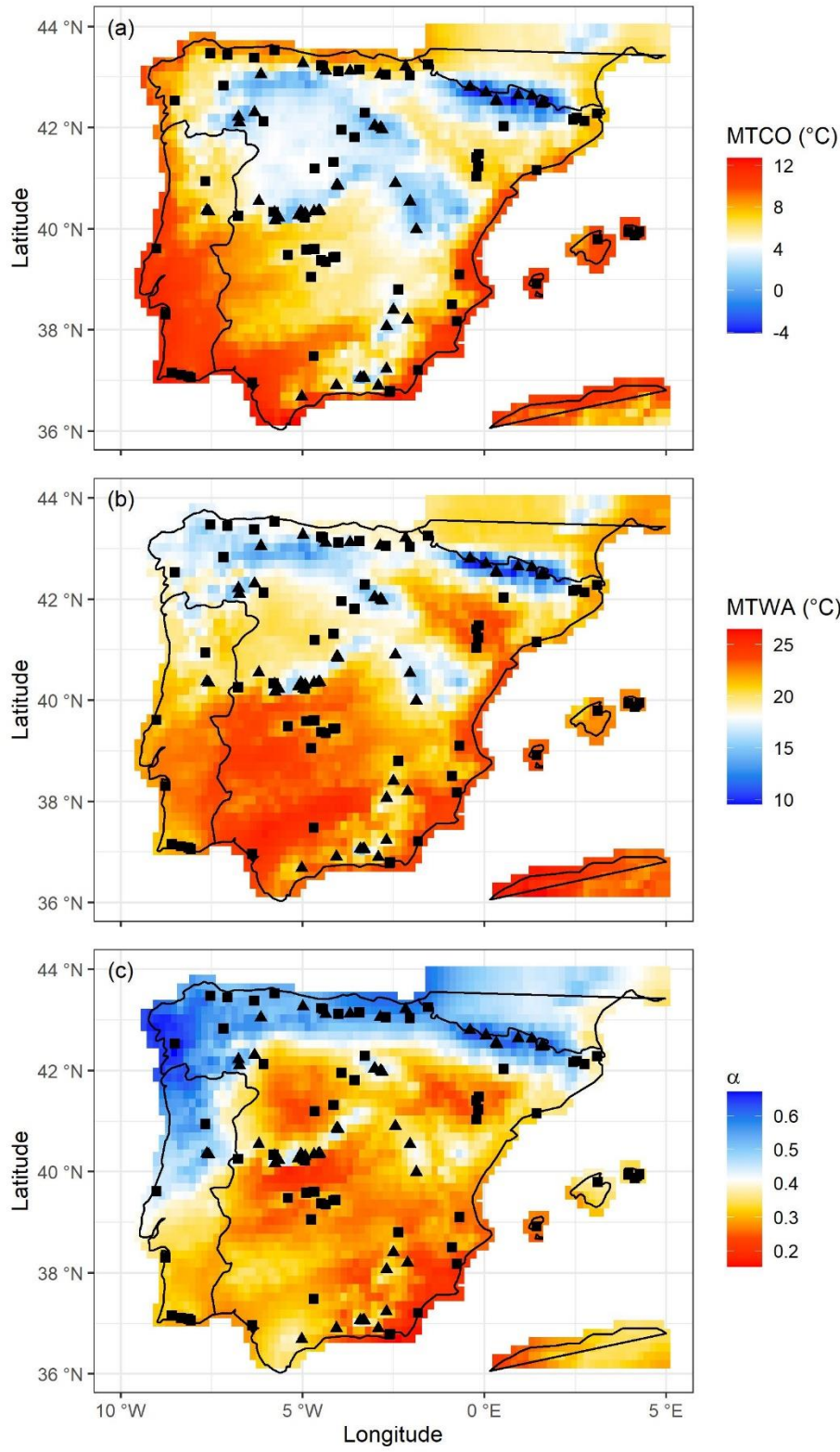
750 Figure 1. Climate space represented by mean temperature of the coldest month (MTCO),
751 mean temperature of the warmest month (MTWA), and plant-available moisture as
752 represented by α , an estimate of the ratio of actual evapotranspiration to equilibrium
753 evapotranspiration. The grey points show climate values for a rectangular area (21° W ~ 150°
754 E, 29° N ~ 82° N) enclosing the SMPDS data set, derived from the Climate Research Unit
755 CRU CL 2.0 database (New et al., 2002). The black points show climate values of the
756 SMPDS dataset. The red points show climate values of the Iberian Peninsula region in the
757 SMPDS dataset.
758



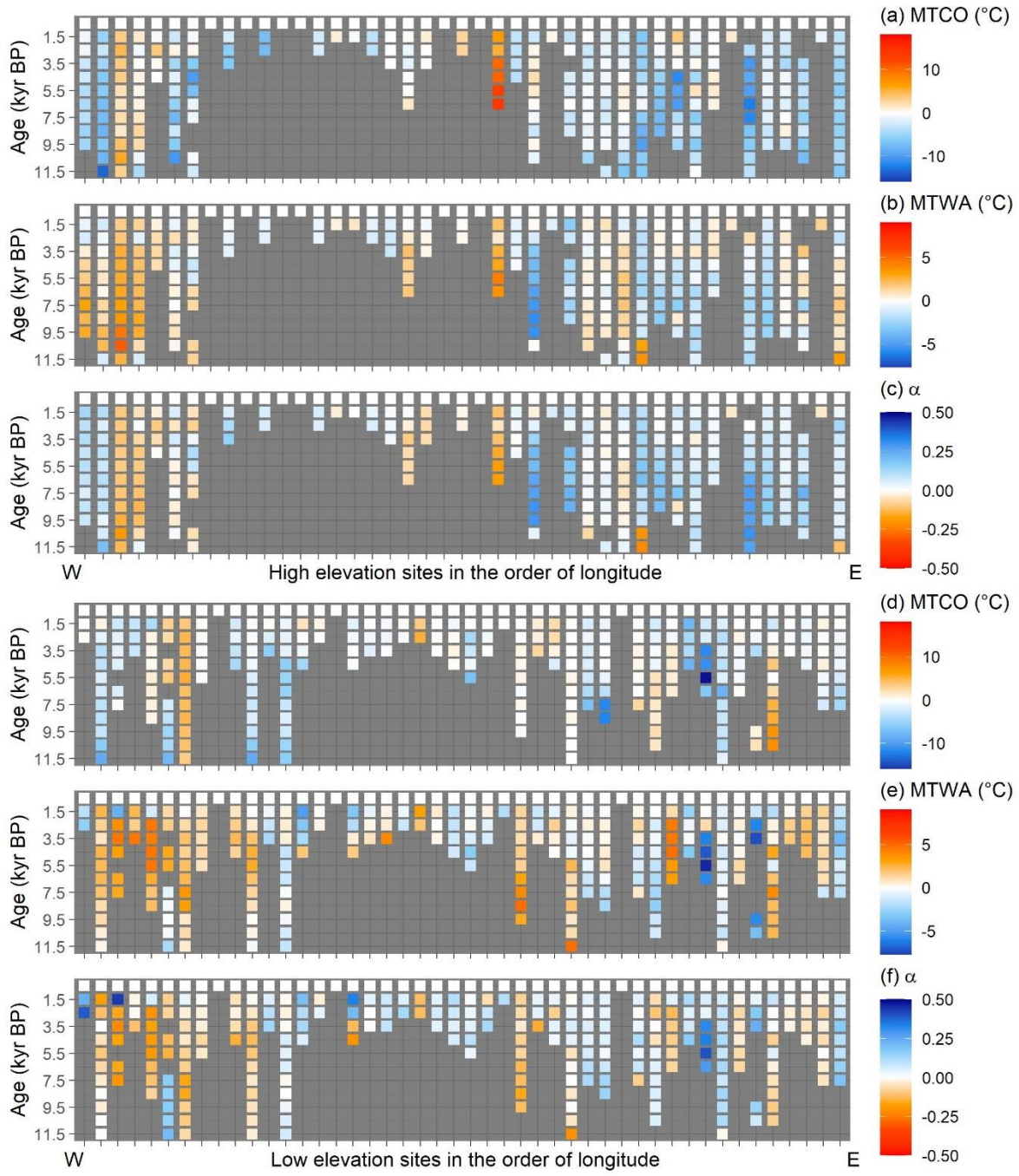
759

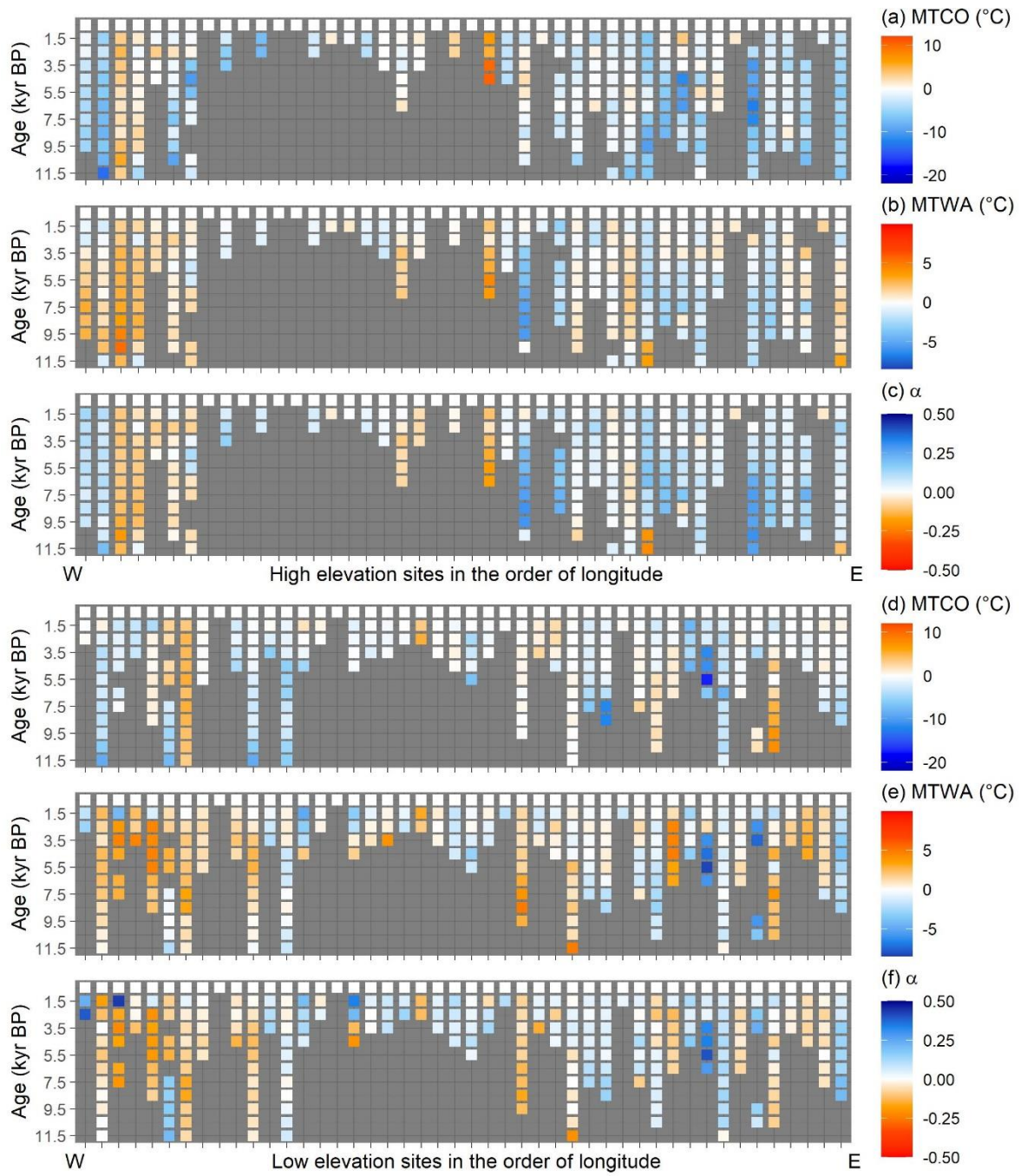
760 Figure 24. Map showing the location of the 117 fossil sites in the Iberian Peninsula used for
761 climate reconstructions. Sites lower than 1000 m above sea level are shown as squares, sites
762 higher than 1000 m above sea level are shown as triangles. The base maps show modern (a)
763 mean temperature of the coldest month (MTCO), (b) mean temperature of the warmest month
764 (MTWA), and (c) plant-available moisture as represented by α , an estimate of the ratio of
765 actual evapotranspiration to equilibrium evapotranspiration.
766



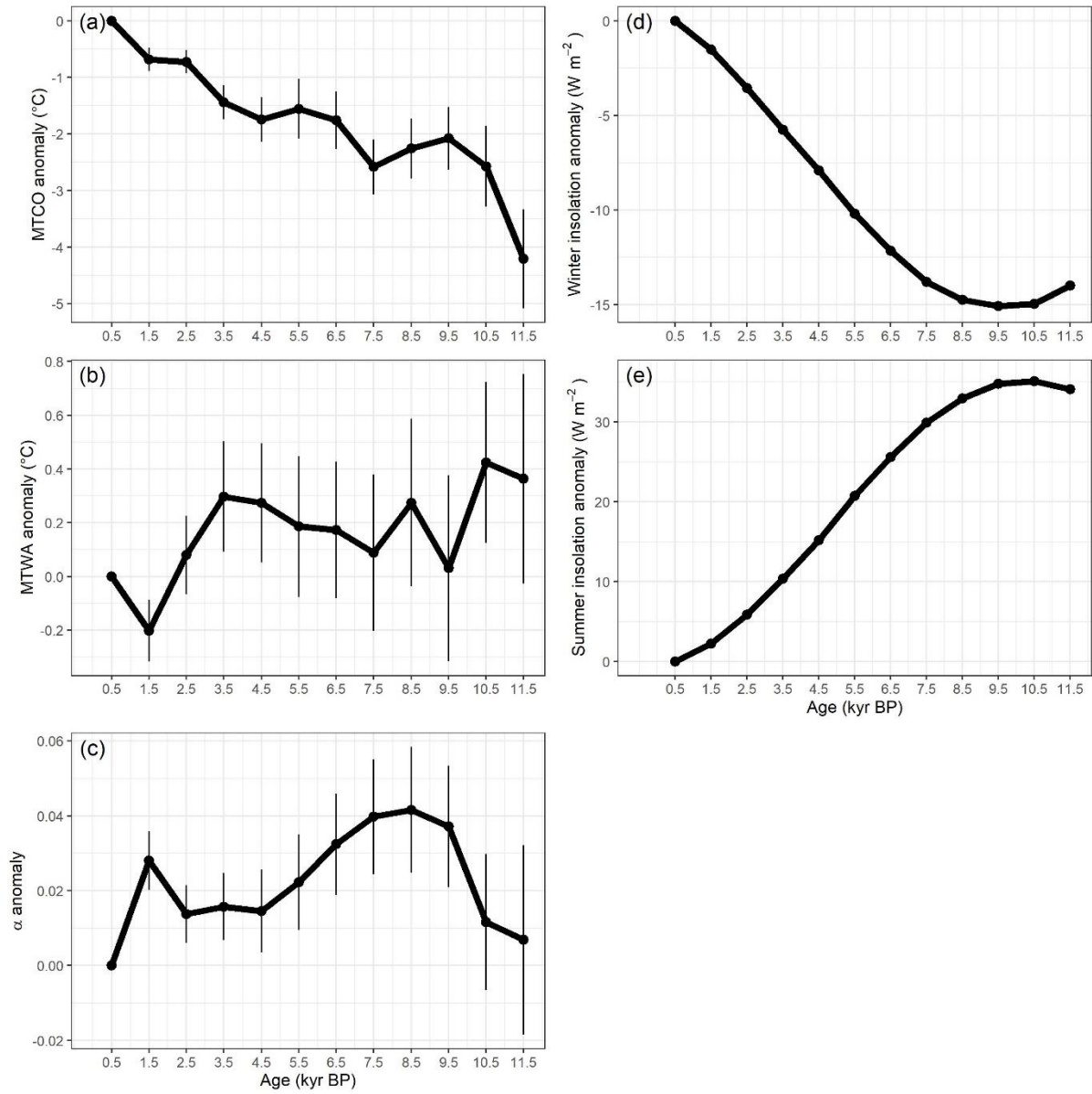


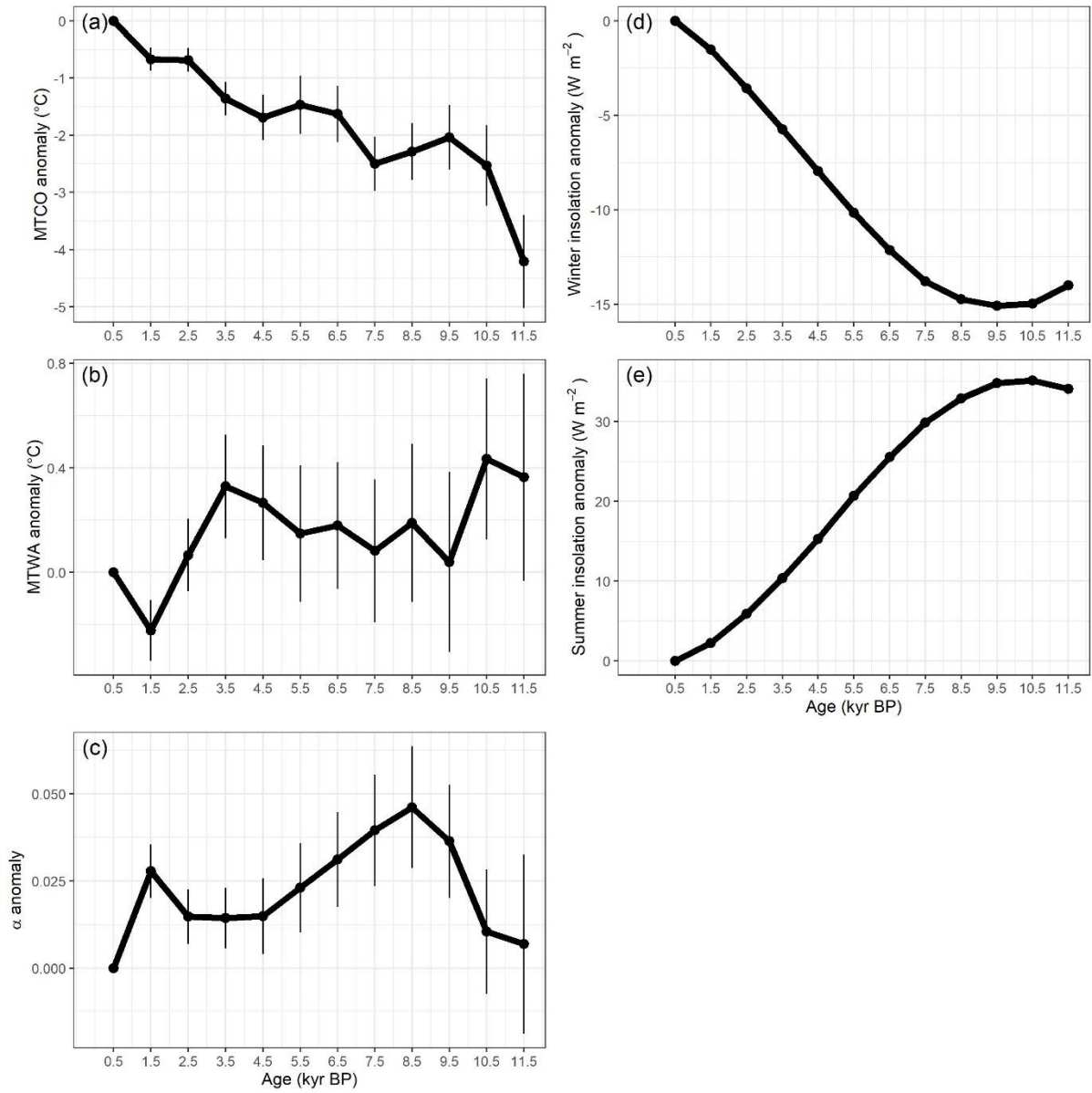
769 Figure 32. Reconstructed anomalies in climate at individual sites through time. The sites are
770 grouped into high (>1000m) and low (<1000m) elevation sites and organised from west to
771 east. Grey cells indicate periods or longitudes with no data. The individual plots show the
772 anomalies in reconstructed (a,d) mean temperature of the coldest month (MTCO), (b,e) mean
773 temperature of the warmest month (MTWA), and (c,f) plant-available moisture as
774 represented by α , an estimate of the ratio of actual evapotranspiration to equilibrium
775 evapotranspiration. The anomalies are expressed as deviations of the mean value in each bin
776 (± 500 years) from the value at 0.5 ka at each site.
777



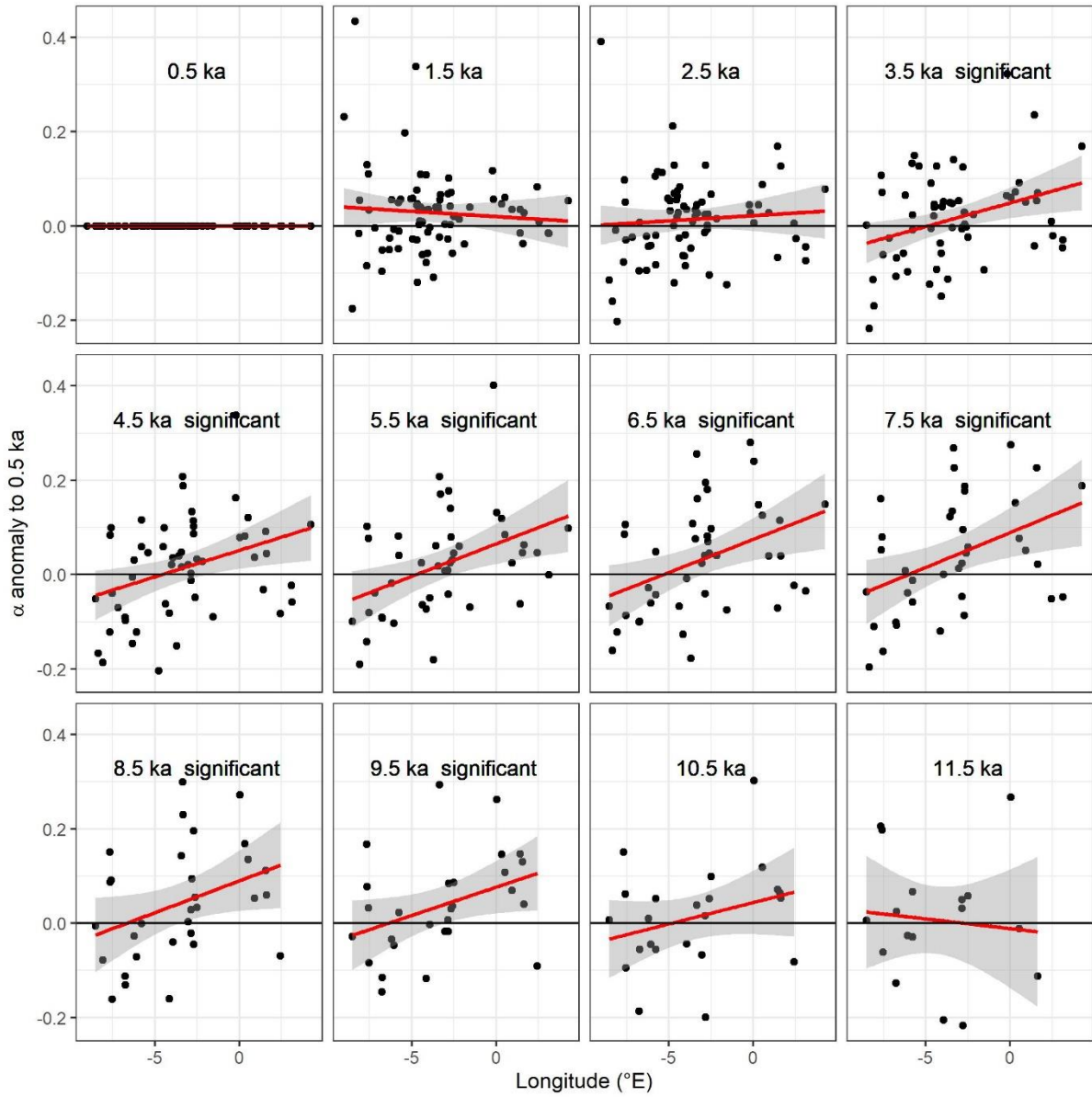


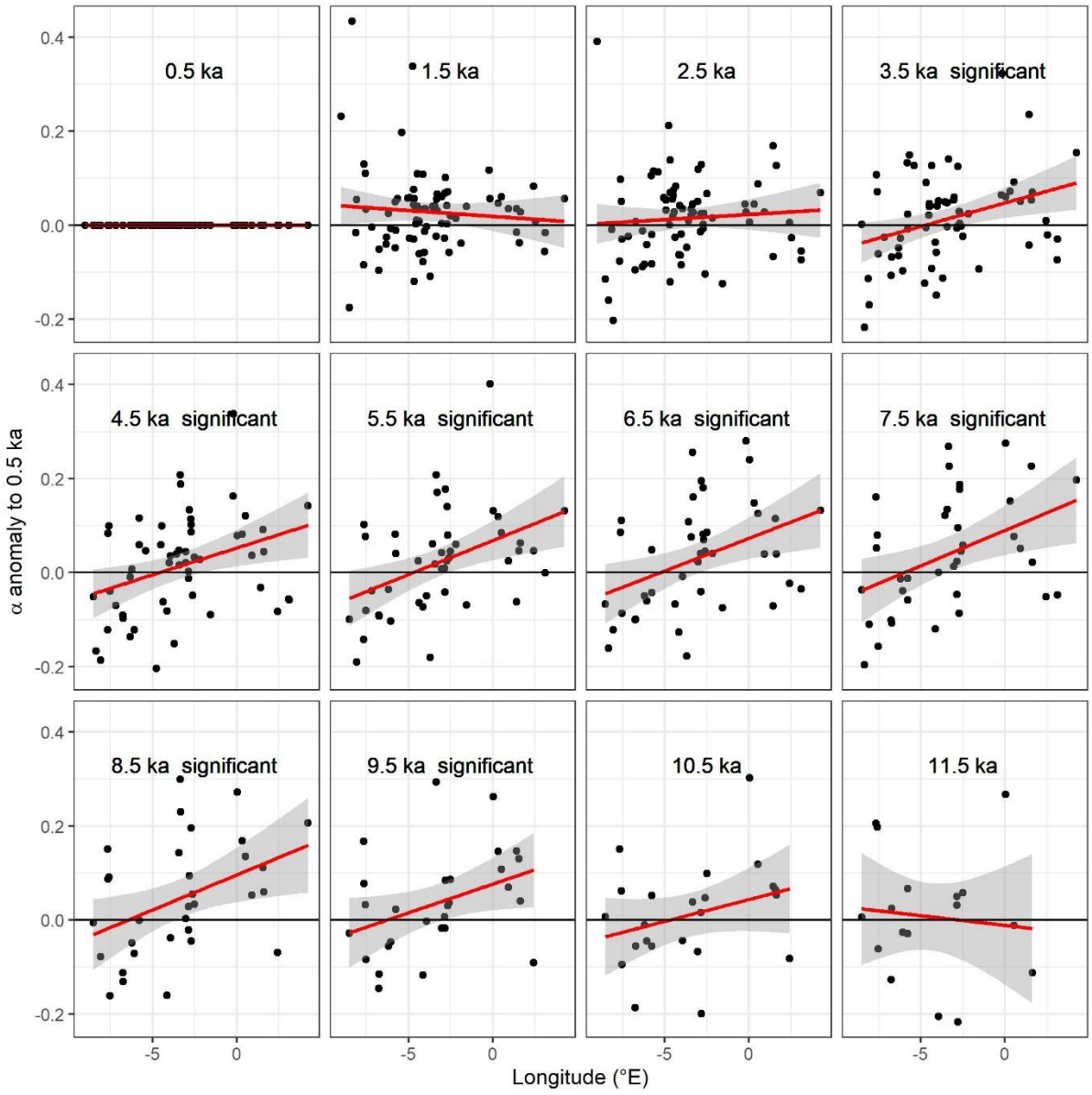
780 Figure 43. Reconstructed composite changes (anomalies to 0.5 ka) in (a) mean temperature of
781 the coldest month (MTCO), (b) mean temperature of the warmest month (MTWA) and (c)
782 plant-available moisture as represented by α , through the Holocene compared to changes in
783 (d) winter and (e) summer insolation for the latitude of the Iberian Peninsula, using ± 500
784 years as the bin. The black lines show mean values across sites, with vertical line segments
785 showing the standard deviations of mean values using 1000 bootstrap cycles of site
786 resampling.
787



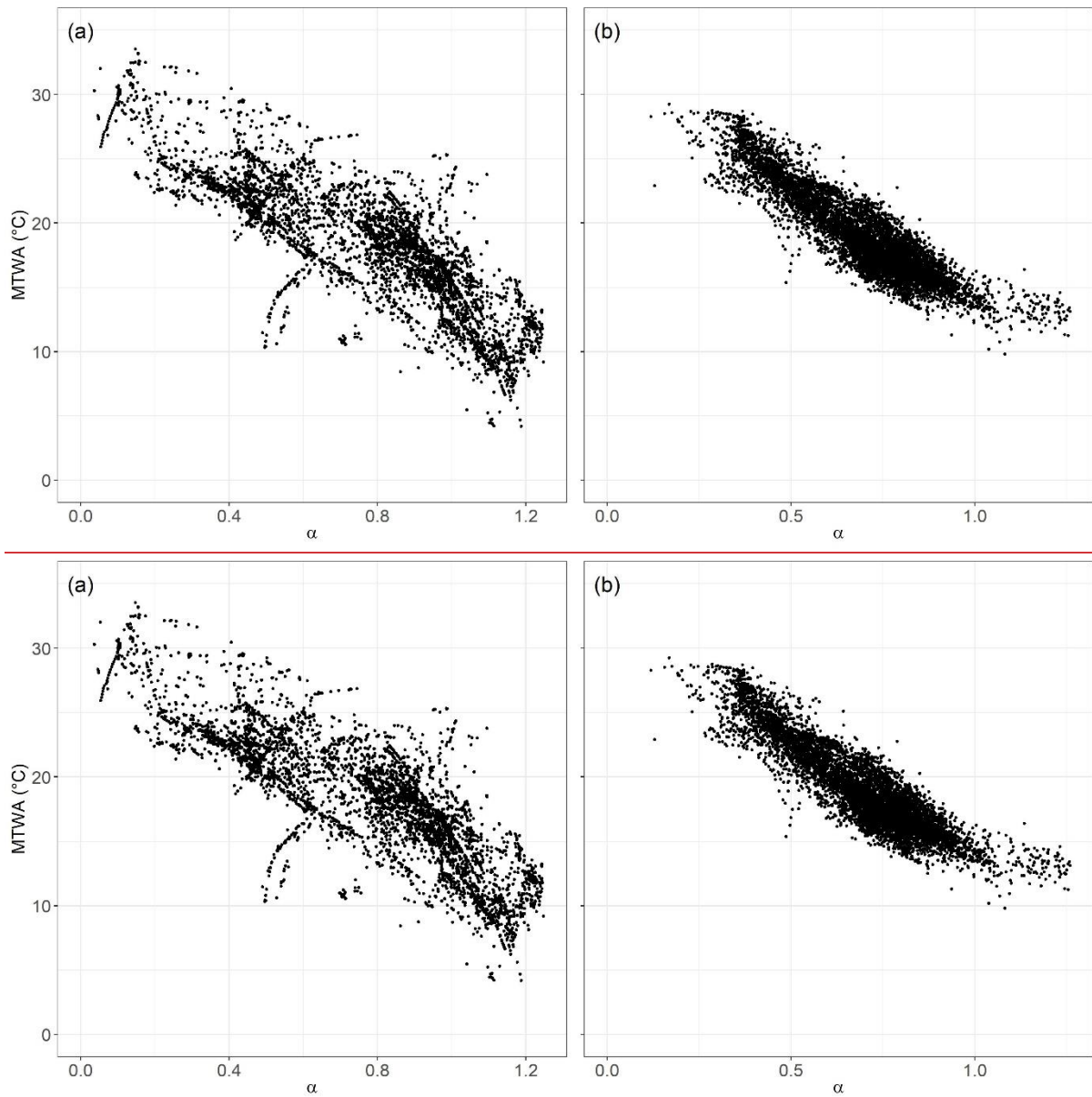


790 Figure 54. Changes in the west-east gradient of plant-available moisture as represented by
791 anomalies in α relative to 0.5 ka at individual sites through the Holocene. The red lines show
792 the regression lines. The shades indicate the 95 % confidence intervals of the regression lines.
793





796 Figure 65. The relationship between mean temperature of the warmest month (MTWA) and
797 plant-available moisture as represented by α (a) in the modern climate data set, and (b) in the
798 Holocene reconstructions.
799



800

801

802 Table 1. Leave-out cross-validation (with geographically and climatically close sites
 803 removed) fitness of the modified version of fxTWA-PLS, for mean temperature of the coldest
 804 month (MTCO), mean temperature of the warmest month (MTWA) and plant-available
 805 moisture (α), with p-spline smoothed fx estimation, using bins of 0.02, 0.02 and 0.002,
 806 showing results for all the components. RMSEP is the root-mean-square error of prediction.
 807 Δ RMSEP is the per cent change of RMSEP using the current number of components than
 808 using one component less. p assesses whether using the current number of components is
 809 significantly different from using one component less, which is used to choose the last
 810 significant number of components (indicated in bold) to avoid over-fitting. The degree of
 811 overall compression is assessed by linear regression of the cross-validated reconstructions
 812 onto the climate variable, b_1 , $b_1.se$ are the slope and the standard error of the slope,
 813 respectively. The closer the slope (b_1) is to 1, the less the overall compression is.
 814
 815

	ncomp	R^2	avg. bias	max. bias	min. bias	RMSEP	Δ RMSEP	p	b_1	$b_1.se$
MTCO	1	0.70	-0.86	25.23	0.00	5.20	-39.97	0.001	0.89	0.01
	2	0.73	-0.73	25.00	0.00	4.87	-6.29	0.001	0.91	0.01
	3	0.74	-0.71	24.38	0.00	4.86	-0.32	0.001	0.91	0.01
	4	0.75	-0.59	24.27	0.00	4.70	-3.26	0.001	0.91	0.01
	5	0.74	-0.63	34.54	0.00	4.77	1.51	1.000	0.91	0.01
MTWA	1	0.52	-0.29	17.13	0.00	3.72	-26.88	0.001	0.69	0.01
	2	0.56	-0.14	17.20	0.00	3.53	-5.06	0.001	0.71	0.01
	3	0.56	-0.13	17.01	0.00	3.53	-0.20	0.008	0.71	0.01
	4	0.57	-0.11	17.30	0.00	3.47	-1.56	0.001	0.71	0.01
	5	0.57	-0.11	17.34	0.00	3.48	0.10	0.780	0.71	0.01
α	1	0.65	-0.014	0.787	0.000	0.165	-39.59	0.001	0.76	0.01
	2	0.68	-0.016	0.781	0.000	0.159	-3.55	0.001	0.77	0.01
	3	0.68	-0.017	0.757	0.000	0.158	-0.61	0.023	0.78	0.01
	4	0.69	-0.017	0.784	0.000	0.158	-0.43	0.108	0.79	0.01
	5	0.69	-0.017	0.850	0.000	0.158	0.26	0.985	0.80	0.01

816

817 Table 2. Canonical Correspondence Analysis (CCA) result of modern and fossil-
 818 reconstructed MTCO, MTWA and α . The summary statistics for the ANOVA-like
 819 permutation test (999 permutations) are also shown. VIF is the variance inflation factor, Df is
 820 the number of degrees of freedom, χ^2 is the constrained eigenvalue (or the sum of
 821 constrained eigenvalues for the whole model)-, F is significance, and Pr (>F) is the
 822 probability.
 823

Modern	Axes	Axis 1	Axis 2	Axis 3	VIF
	Constrained eigenvalues	0.3819	0.1623	0.1087	/
	Correlations of the environmental variables with the axes:				
	MTCO	-0.815	0.579	0.012	1.31
	MTWA	-0.700	-0.203	0.685	3.34
	α	0.883	0.430	-0.187	3.39
		Df	χ^2	F	Pr (>F)
	Whole model	3	0.6530	78.113	0.001
	MTCO	1	0.3082	110.597	0.001
	MTWA	1	0.1602	57.489	0.001
	α	1	0.1846	66.252	0.001
	CCA 1	1	0.3819	137.076	0.001
	CCA 2	1	0.1623	58.252	0.001
CCA 3	1	0.1087	39.011	0.001	
Fossil-reconstructed	Axes	Axis 1	Axis 2	Axis 3	VIF
	Constrained eigenvalues	<u>0.3601</u> 0.3594	<u>0.2266</u> 0.2270	<u>0.2037</u> 0.2043	/
	Correlations of the environmental variables with the axes:				
	MTCO	<u>0.430</u> -0.417	<u>0.776</u> -0.767	<u>0.462</u> 0.488	<u>1.34</u> 1.33
	MTWA	<u>0.987</u> -0.987	<u>0.141</u> -0.146	<u>-0.076</u> -0.068	<u>5.40</u> 5.31
	α	<u>-0.947</u> -0.945	<u>0.088</u> 0.095	<u>-0.308</u> -0.311	<u>5.285</u> .19
		Df	χ^2	F	Pr (>F)
	Whole model	3	<u>0.7905</u> 0.7906	<u>226.98</u> 225.12	0.001
	MTCO	1	<u>0.2465</u> 0.2446	<u>212.34</u> 208.91	0.001
	MTWA	1	<u>0.329</u> 0.330 9	<u>284.07</u> 282.65	0.001
	α	1	<u>0.214</u> 0.215 2	<u>184.53</u> 183.79	0.001
	CCA 1	1	<u>0.360</u> 0.359 4	<u>310.19</u> 307.00	0.001
	CCA 2	1	<u>0.2266</u> 0.2270	<u>195.24</u> 193.88	0.001
CCA 3	1	<u>0.2037</u> 0.204 3	<u>175.51</u> 174.48	0.001	

825 Table 3. Assessment of the significance of anomalies to 0.5 ka through time with latitude and
 826 elevation. The slope is obtained by linear regression of the anomaly onto the longitude or
 827 elevation. p is the significance of the slope (bold parts: $p < 0.05$). x_0 is the point where the
 828 anomaly is 0 in the linear equation, which indicates longitude or elevation where the anomaly
 829 changes sign.
 830

		Longitude (°E)			Elevation (km)		
	age (ka)	slope	p	x_0	slope	p	x_0
MTCO (°C)	0.5	0.000-0.00	//	//	0.000-0.00	//	//
	1.5	-0.07-0.07	<u>0.4110-453</u>	-13.02-13-80	-0.30-0.39	<u>0.4110-285</u>	-1.21-0.71
	2.5	-0.15-0.14	<u>0.0950-113</u>	-8.56-8.52	-0.52-0.52	<u>0.1790-170</u>	-0.40-0.29
	3.5	-0.13-0.14	<u>0.3140-253</u>	-14.83-13-06	-0.81-0.79	<u>0.1420-147</u>	-0.77-0.72
	4.5	-0.12-0.12	<u>0.4440-445</u>	-17.28-16-97	-0.69-0.69	<u>0.3190-315</u>	-1.46-1.37
	5.5	-0.24-0.24	<u>0.2470-260</u>	-9.49-9-37	-0.61-0.63	<u>0.5030-477</u>	-1.43-1.17
	6.5	-0.18-0.17	<u>0.3720-405</u>	-12.74-12-79	-0.87-0.88	<u>0.2930-281</u>	-0.88-0.71
	7.5	-0.15-0.16	<u>0.4210-391</u>	-20.39-18-89	-1.38-1.43	<u>0.0800-067</u>	-0.67-0.55
	8.5	-0.03-0.08	<u>0.8900-703</u>	-77.87-33-59	-1.58-1.34	<u>0.0650-101</u>	-0.10-0.42
	9.5	<u>0.010-0.00</u>	<u>0.9540-992</u>	<u>156.31937-82</u>	-1.79-1.81	<u>0.0600-056</u>	<u>0.110-14</u>
	10.5	<u>0.200-19</u>	<u>0.4740-493</u>	<u>9.259-85</u>	-1.38-1.38	<u>0.2410-232</u>	-0.64-0.62
	11.5	<u>0.230-23</u>	<u>0.5280-528</u>	<u>13.7713-77</u>	<u>0.120-12</u>	<u>0.9470-947</u>	<u>36.3536-35</u>
MTWA (°C)	0.5	0.000-0.00	//	//	0.000-0.00	//	//
	1.5	-0.010-0.00	<u>0.8620-928</u>	-26.38-51-95	-0.05-0.04	<u>0.8300-859</u>	-3.35-4.94
	2.5	-0.09-0.09	<u>0.1370-164</u>	-2.80-2-90	-0.45-0.48	<u>0.0920-069</u>	<u>1.191-15</u>
	3.5	-0.23-0.22 2	<u>0.0050-0.00</u> 7	-2.03-1-8 4	-0.40-0.44	<u>0.2840-236</u>	<u>1.741-76</u>
	4.5	-0.21-0.22 2	<u>0.0160-0.01</u> 4	-2.01-2-0 8	-0.58-0.57	<u>0.1260-140</u>	<u>1.551-56</u>
	5.5	-0.26-0.22 9	<u>0.0110-0.00</u> 5	-2.43-2-6 2	-0.49-0.43	<u>0.2800-340</u>	<u>1.531-49</u>
	6.5	-0.24-0.22 4	<u>0.0170-0.01</u> 5	-2.30-2-2 8	-0.62-0.61	<u>0.1370-134</u>	<u>1.411-43</u>
	7.5	-0.26-0.22 7	<u>0.0120-0.01</u> 0	-3.02-3-0 5	-1.05-1-0 3	<u>0.0190-0.02</u> 1	<u>1.281-28</u>
	8.5	-0.24-0.26	<u>0.0610-0.024</u>	-2.43-2-62	-1.15-0-8 7	<u>0.0230-0.07</u> 9	<u>1.571-51</u>
	9.5	-0.32-0-3 2	<u>0.0130-0.01</u> 2	-3.20-3-1 7	-0.44-0.44	<u>0.4590-457</u>	<u>1.341-36</u>
	10.5	-0.18-0.18	<u>0.1150-110</u>	-1.23-1-21	<u>0.540-54</u>	<u>0.2760-278</u>	<u>0.440-42</u>

	11.5	0.130.13	0.4530.453	-7.25-7.25	0.370.37	0.6630.663	0.220.22
α	0.5	0.000.00	∕	∕	0.000.00	∕	∕
	1.5	0.000.00	0.5080.453	8.997.55	-0.01-0.01	0.3930.438	3.403.67
	2.5	0.000.00	0.5170.526	-9.89-10.4 1	0.020.02	0.2490.211	0.190.21
	3.5	0.010.01	0.0060.00 6	-4.91-4.7 8	0.020.02	0.1910.161	0.280.38
	4.5	0.010.01	0.0100.00 9	-4.60-4.6 0	0.050.05	0.0080.00 8	0.790.79
	5.5	0.010.01	0.0050.00 3	-4.75-4.7 3	0.050.05	0.0270.03 1	0.670.65
	6.5	0.010.01	0.0070.00 7	-5.34-5.2 8	0.060.06	0.0040.00 3	0.600.64
	7.5	0.020.02	0.0090.00 8	-6.05-5.9 9	0.090.09	0.0000.00 0	0.750.75
	8.5	0.010.02	0.0490.01 8	-6.67-6.4 5	0.090.08	0.0000.00 4	0.880.68
	9.5	0.010.01	0.0480.04 6	-6.40-6.2 9	0.070.07	0.0120.01 2	0.700.72
	10.5	0.010.01	0.1830.173	-4.85-4.70	0.020.02	0.5350.523	0.590.67
	11.5	0.000.00	0.7130.713	-2.76-2.76	0.030.03	0.6540.654	0.930.93

832 **Appendix A**833 **Theoretical basis:**834 **The previous version of fxTWA-PLS (fxTWA-PLS1):**

835 The estimated optimum (\hat{u}_k) and unbiased tolerance (\hat{t}_k) of each taxon are calculated from
836 the modern training data set as follows:

$$837 \quad \hat{u}_k = \frac{\sum_{i=1}^n y_{ik} x_i}{\sum_{i=1}^n y_{ik}} \quad (A1)$$

$$838 \quad \hat{t}_k = \sqrt{\frac{\sum_{i=1}^n y_{ik} (x_i - \hat{u}_k)^2}{(1 - 1/N_{2k}) \sum_{i=1}^n y_{ik}}} \quad (A2)$$

839 where

$$840 \quad N_{2k} = \frac{1}{\sum_{i=1}^n \left(\frac{y_{ik}}{\sum_{i'=1}^n y_{i'k}} \right)^2} \quad (A3)$$

841 where n is the total number of sites; y_{ik} is the observed abundance of the k^{th} taxon at the i^{th}
842 site; x_i is the observed climate value at the i^{th} site; N_{2k} is the effective number of occurrences
843 for the k^{th} taxon.

844 fx correction is applied as weight in the form of $1/f_{x^2}$ at regression at step 7 in Table 1 in Liu
845 et al. (2020). The regression step uses robust linear model fitting by the R code:

$$847 \quad rlm(x_i \sim comp_1 + comp_2 + \dots + comp_{pls}, weights = 1/f_{x^2}) \quad (A4)$$

848

849 **The modified version of fxTWA-PLS (fxTWA-PLS2):**

850 The distribution of y_{ik} is influenced by the distribution of the climate variable, so we need to
851 apply the fx correction when calculating optimum and tolerance for each taxon as follows:

$$852 \quad \hat{u}_k = \frac{\sum_{i=1}^n \frac{y_{ik} x_i}{f_{x_i}}}{\sum_{i=1}^n \frac{y_{ik}}{f_{x_i}}} \quad (A5)$$

$$853 \quad \hat{t}_k = \sqrt{\frac{\sum_{i=1}^n \frac{y_{ik} (x_i - \hat{u}_k)^2}{f_{x_i}}}{\left(1 - \frac{1}{N_{2k}}\right) \sum_{i=1}^n \frac{y_{ik}}{f_{x_i}}}} \quad (A6)$$

854 where

$$855 \quad N_{2k} = \frac{1}{\sum_{i=1}^n \left(\frac{\frac{y_{ik}}{f_{x_i}}}{\sum_{i'=1}^n \frac{y_{i'k}}{f_{x_{i'}}}} \right)^2} \quad (A7)$$

856 The modified version of fxTWA-PLS applies fx correction separately at taxon calculation
857 and regression (step 2 and 7 in Table 1 in Liu et al., 2020), both using weight in the form of
858 $1/f_x$. The regression step (step 7) then becomes:

$$859 \quad rlm(x_i \sim comp_1 + comp_2 + \dots + comp_{pls}, weights = 1/fx) \quad (A8)$$

860 The previous version uses fx values extracted from histograms, and different bin widths may
861 result in different training results. The modified version applies P-splines histogram
862 smoothing (Eilers and Marx, 2021) with third order difference penalty, which makes the fx
863 values almost independent on the bin width. The optimal smoothing parameter of the P-spline
864 penalty was determined by the HFS (Harville-Fellner-Schall) algorithm (Eilers and Marx,
865 2021) for the Poisson likelihood for the histogram counts.

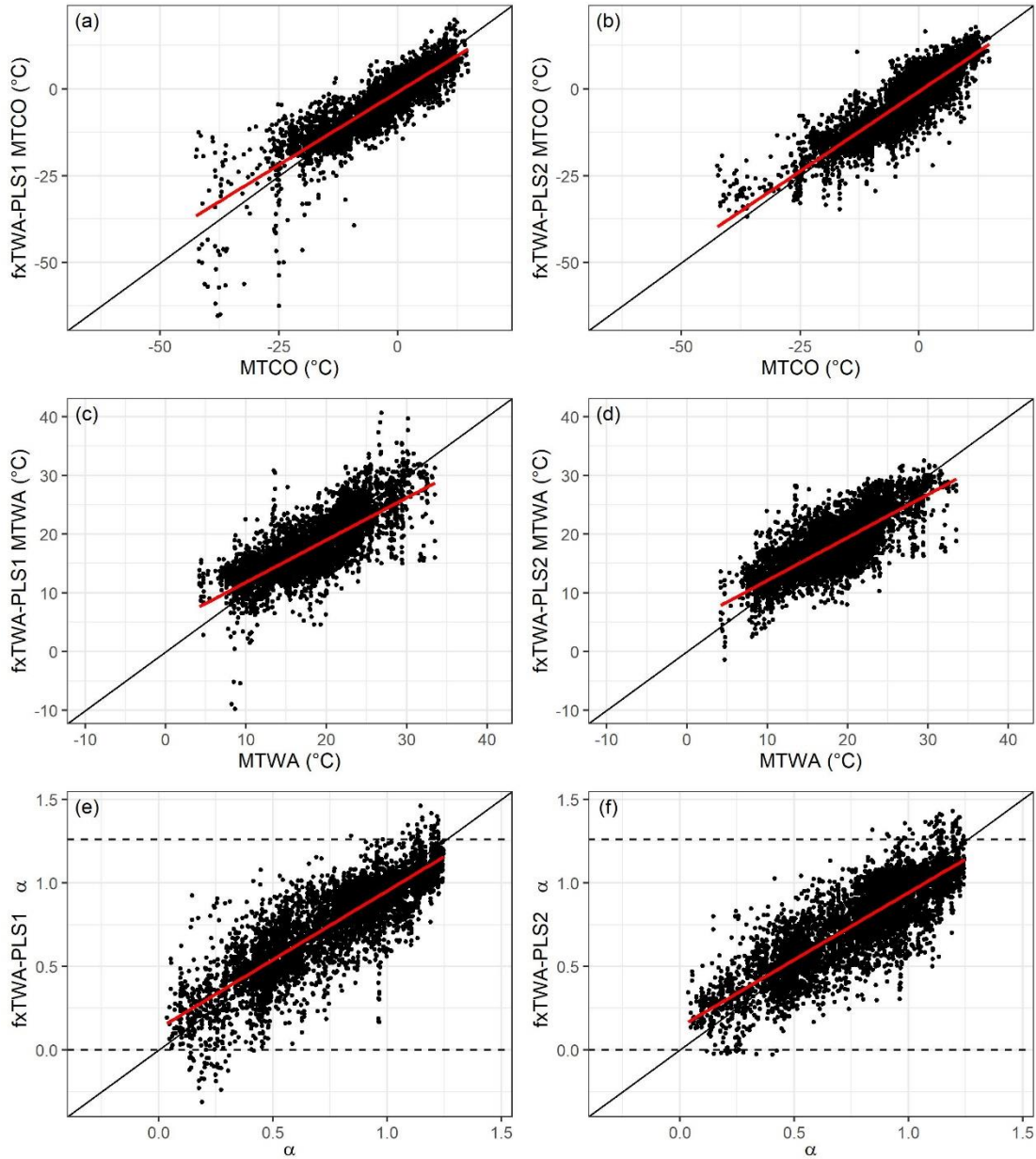
866 Table A1. Leave-out cross-validation (with geographically and climatically close sites removed)
 867 fitness of the previous and modified version of fxTWA-PLS (fxTWA-PLS1 and fxTWA-PLS2,
 868 respectively), for mean temperature of the coldest month (MTCO), mean temperature of the warmest
 869 month (MTWA) and plant-available moisture (α), using bins of 0.02, 0.02 and 0.002, respectively. n
 870 is the number of components used. RMSEP is the root mean square error of prediction. Δ RMSEP is
 871 the per cent change of RMSEP using the current number of components than using one component
 872 less. p assesses whether using the current number of components is significantly different from using
 873 one component less, which is used to choose the last significant number of components (indicated in
 874 bold) to avoid overfitting. The degree of overall compression is assessed by doing linear regression to
 875 the cross-validation result and the climate variable. b_1 , $b_1.se$ are the slope and the standard error of
 876 the slope, respectively. The closer the slope (b_1) is to 1, the lower the overall compression is. fx
 877 correction is set intrinsic in functions in `fxTWA` package for both versions in this paper, instead
 878 of relying on an outside input in Liu et al. (2020), so the values of fxTWA-PLS1 might be slighted
 879 different from values in Table 2 in Liu et al. (2020), but it doesn't affect the conclusion.
 880

	Method	n	R^2	avg. bias	max. bias	min. bias	RMSEP	Δ RMSEP	p	b_1	$b_1.se$
MTCO	fxTWA-PLS1	1	0.66	-0.86	31.17	0.00	5.21	-39.87	0.001	0.76	0.01
		2	0.72	-0.52	36.65	0.00	4.70	-9.78	0.001	0.80	0.01
		3	0.73	-0.47	41.18	0.00	4.62	-1.63	0.001	0.82	0.01
		4	0.73	-0.51	44.86	0.00	4.58	-1.01	0.006	0.82	0.01
		5	0.73	-0.41	58.35	0.00	4.62	0.89	0.708	0.83	0.01
	fxTWA-PLS2	1	0.70	-0.86	25.23	0.00	5.20	-39.97	0.001	0.89	0.01
		2	0.73	-0.73	25.00	0.00	4.87	-6.29	0.001	0.91	0.01
		3	0.74	-0.71	24.38	0.00	4.86	-0.32	0.001	0.91	0.01
		4	0.75	-0.59	24.27	0.00	4.70	-3.26	0.001	0.91	0.01
		5	0.74	-0.63	34.54	0.00	4.77	1.51	1.000	0.91	0.01
MTWA	fxTWA-PLS1	1	0.50	-0.53	17.91	0.00	3.87	-24.09	0.001	0.67	0.01
		2	0.56	-0.54	17.71	0.00	3.52	-8.98	0.001	0.69	0.01
		3	0.57	-0.49	25.14	0.00	3.52	0.09	0.565	0.73	0.01
		4	0.57	-0.43	34.92	0.00	3.56	1.12	0.974	0.75	0.01
		5	0.57	-0.46	32.23	0.00	3.55	-0.23	0.139	0.74	0.01
	fxTWA-PLS2	1	0.52	-0.29	17.13	0.00	3.72	-26.88	0.001	0.69	0.01
		2	0.56	-0.14	17.20	0.00	3.53	-5.06	0.001	0.71	0.01
		3	0.56	-0.13	17.01	0.00	3.53	-0.20	0.008	0.71	0.01
		4	0.57	-0.11	17.30	0.00	3.47	-1.56	0.001	0.71	0.01
		5	0.57	-0.11	17.34	0.00	3.48	0.10	0.780	0.71	0.01
α	fxTWA-PLS1	1	0.63	-0.020	0.773	0.000	0.174	-36.23	0.001	0.78	0.01
		2	0.69	-0.012	0.902	0.000	0.157	-9.66	0.001	0.79	0.01
		3	0.69	-0.011	0.820	0.000	0.155	-1.28	0.001	0.79	0.01
		4	0.70	-0.010	0.786	0.000	0.156	0.25	0.867	0.81	0.01
		5	0.70	-0.010	0.786	0.000	0.156	0.09	1.000	0.81	0.01
	fxTWA-PLS2	1	0.65	-0.014	0.787	0.000	0.165	-39.59	0.001	0.76	0.01
		2	0.68	-0.016	0.781	0.000	0.159	-3.55	0.001	0.77	0.01
		3	0.68	-0.017	0.757	0.000	0.158	-0.61	0.023	0.78	0.01
		4	0.69	-0.017	0.784	0.000	0.158	-0.43	0.108	0.79	0.01
		5	0.69	-0.017	0.850	0.000	0.158	0.26	0.985	0.80	0.01

881

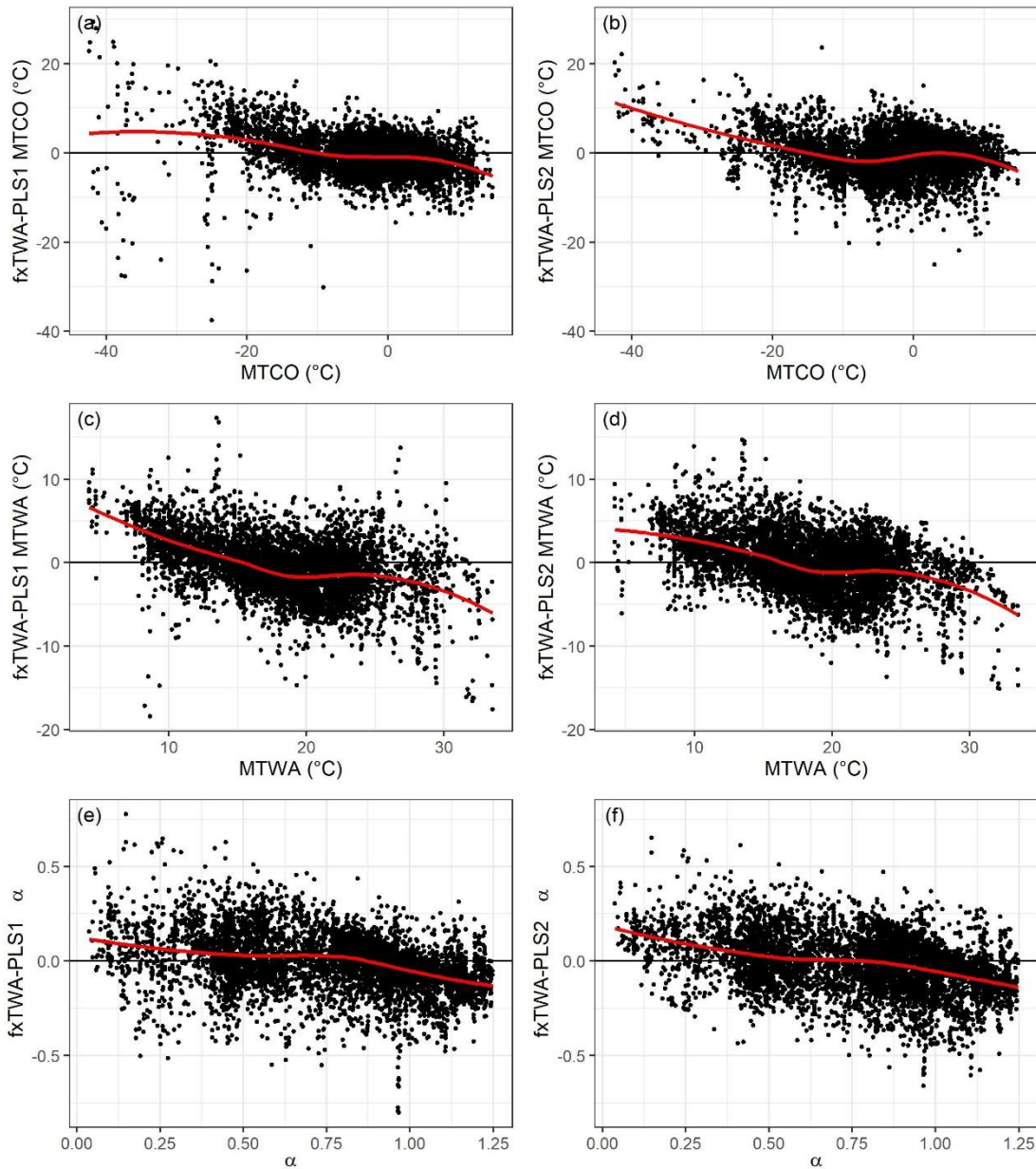
882

883 Figure A1. Training results using the last significant number of components. The left panel
 884 shows the previous version (fxTWA-PLS1) and the right panel shows the modified version of
 885 fxTWA-PLS (fxTWA-PLS2). The 1: 1 line is shown in black; the linear regression line is
 886 shown in red, to show the degree of overall compression. The horizontal dashed lines indicate
 887 the natural limit of α (0~1.26).
 888



889
 890

891 Figure A2. Residuals using the last significant number of components. The left panel shows
 892 the previous version (fxTWA-PLS1) and the right panel shows the modified version (fxTWA-
 893 PLS2) of fxTWA-PLS. The zero line is shown in black; the locally estimated scatterplot
 894 smoothing is shown in red, to show the degree of local compression.
 895



896

897 As shown in Table A1, Figure A1 and A2, the modified version is able to further reduce the
 898 compression in MTCO and MTWA, and maximum bias in MTCO, MTWA and α . As shown
 899 in Figure A1 and A2, there is less scatter and there are less α values beyond the natural limit.